Fall 1-2021

Relative Pose Uncertainty Quantification Using Lie Group Variational Filtering

Christopher W. Hays
Embry-Riddle Aeronautical University, chriswhays@gmail.com

RELATIVE POSE UNCERTAINTY QUANTIFICATION USING LIE GROUP VARIATIONAL FILTERING

By

Christopher W. Hays

A Thesis Submitted to the Faculty of Embry-Riddle Aeronautical University

In Partial Fulfillment of the Requirements for the Degree of

Master of Science in Aerospace Engineering

January 2021

Embry-Riddle Aeronautical University

Daytona Beach, Florida

RELATIVE POSE UNCERTAINTY QUANTIFICATION USING LIE GROUP VARIATIONAL FILTERING

By

Christopher W. Hays

This Thesis was prepared under the direction of the candidate's Thesis Committee Chair, Dr. Troy Henderson, Department of Aerospace Engineering, and has been approved by the members of the Thesis Committee. It was submitted to the Office of the Senior Vice President for Academic Affairs and Provost, and was accepted in the partial fulfillment of the requirements for the Degree of Master of Science in Aerospace Engineering.

THESIS COMMITTEE

Troy A. Henderson Digitally signed by Troy A. Henderson Date: 2021.01.19 15:50:32 -05'00'

Chairman, Dr. Troy Henderson

Morad Nazari Digitally signed by Morad Nazari Date: 2021.01.19 15:53:50 -05'00'

Member, Dr. Morad Nazari

Richard J. Prazenica Digitally signed by Richard J. Prazenica Date: 2021.01.19 16:04:38 -05'00'

Member, Dr. Richard Prazenica

Marwan Al-Haik Digitally signed by Marwan Al-Haik DN: cn=Marwan Al-Haik, o=Embry-Riddle Aeronautical University, ou=Aerospace Engineering, email=alhaikm@erau.edu, c=US Date: 2021.01.19 16:09:48 -05'00'

Graduate Program Coordinator, Dr. Marwan Al-Haik

Date

Maj Mirmirani Digitally signed by Maj Mirmirani Date: 2021.01.19 16:30:31 -05'00'

Dean of the College of Engineering, Dr. Maj Mirmirani

Date

Christopher Grant Digitally signed by Christopher Grant Date: 2021.01.19 16:54:08 -05'00'

Associate Provost of Academic Support, Dr. Christopher Grant

Date

ACKNOWLEDGEMENTS

The heavens declare the glory of God...

- Psalm 19:1

First and foremost, I thank God for granting me the ability and opportunity to pursue my passions. I want to thank Dr. Troy Henderson for allowing me to work under his supervision and providing me with opportunity to pursue exciting new research in the field of space navigation. Additionally, I want to thank my committee Dr. Morad Nazari, and Dr. Richard Prazenica for sparking my interest in Geometric Mechanics and visual sensing for space-based navigation.

Working out of the Space Technologies has introduced me to a number of wonderful people who have contributed to the fruition of this work through stimulating debate and distracting conversation. Each of which were equally important to the success of this work. To Daniel Posada, Madhur Tiwari, and David Zuehlke, thank you.

Last, and certainly not least, I want to thank my family. To my parents, Ron and Regina, thank you for all of the sacrifices you have made and the support you have given me to get me to where I am today. To my wife, Torii, thank you for reminding me daily that life is not about the work I do, but the people I connect with while doing it.

ABSTRACT

The applications of visual sensing techniques have revolutionized the way autonomous systems perceive their environment on Earth. In space, the challenge of accurate perception has proven to be a difficult task. Due to adverse lighting conditions, high-noise images are common and degrade the performance of traditional feature-based estimation and perception algorithms. This work explores the applications of a variational filtering scheme founded in Lie Group theory to an autonomous rendezvous, proximity operations and docking problem. Two methodologies, a Monte Carlo approach and an Unscented Transform, for propagating uncertainty using a Lie Group Variational Filter are introduced and developed.

TABLE OF CONTENTS

LIST OF FIGURES

Figure Page

ABBREVIATIONS

SLAM	Simultaneous Localization and Mapping
ARPOD	Autonomous Rendezvous, Proximity Operations, and Docking
LEO	Low-Earth Orbit
ISS	International Space Station
OpNav	Optical Navigation
RPO	Rendezvous and Proximity Operations
SIFT	Scale-Invariant Feature Transform
SURF	Speeded Up Robust Feature
ORB	Oriented FAST and rotated BRIEF
DART	Demonstrate Autonomous Rendezvous Technology
DARPA	Defense Advanced Research Projects Agency
ALHAT	Autonomous Landing Hazard Avoidance Technology
TRN	Terrain Relative Navigation
HDA	Hazard Detection and Avoidance
SPHERES	Synchronized Position Hold Engage and Reorient Experimental Satellites
NASA	National Aeronautics and Space Administration
LiDAR	Light Detection and Ranging
IMU	Inertial Measurement Unit
EKF	Extended Kalman Filter
PHD	Probability Hypothesis Density Filter
LGVF	Lie Group Variational Filter
GPS	Global Positioning System

NOMENCLATURE

$\boldsymbol{\chi}$	An Element on a Manifold $\mathcal{M}$
$\boldsymbol{\nu}$	Translational Velocity
$\boldsymbol{\Omega}$	Angular Velocity
$\boldsymbol{\Sigma}$	Covariance Matrix Formed From Elements of $\mathfrak{se}(3)$
$\boldsymbol{\tau}$	An Element on a Lie algebra $\mathfrak{m}$
$\boldsymbol{\xi}$	An Element on $\mathfrak{se}(3)$ Representing a Disturbance
ϵ	Identity Element
$\mathbb{D}$	Rayleigh Dissipation Terms
$\mathbb{J}$	Artificial Inertial-like Kernel Matrix for Estimator Tuning
$\mathcal{M}$	An Example Lie group
$\mathfrak{m}$	An Example Lie algebra
$\mathfrak{se}(3)$	Lie algebra of $SE(3)$
$\mathfrak{so}(3)$	Lie algebra of $SO(3)$
G	An Element of $SE(3)$
R	An Element of $SO(3)$
T	An Element of $SE(3)$
I	Identity Matrix
J	Moment of Inertia Matrix
M	Mass Matrix
O	Inertial Reference Frame
S	Chaser Spacecraft Body Frame
$SE(3)$	Special Euclidean Group of the 3rd dimension
$SO(3)$	Special Orthogonal Group of the 3rd dimension
L	Lagrangian
T	Kinetic Energy
U	Potential Energy
a	Feature Point position in Frame S

b	Position of Frame S with respect to Frame O
d	Feature Point Position With Respect to a Reference Feature Expressed in Frame O
h	Estimation Error Expressed in $SE(3)$
l	Feature Point Position With Respect to a Reference Feature Expressed in Frame S
P	Covariance Matrix
p	Feature Point position in Frame O
Q	Attitude Estimation Error
V	Augmented Velocity
y	Position Estimation Error

1. Introduction

Typically, the infrastructure for successful space-based operations requires extensive utilization of ground-based assets. The limited availability of these resources restricts the capabilities of space operations on a large scale. Specifically, missions that require significant amounts of decision-making and data analysis consume a considerable amount of ground-based support. As the frequency and scale of these missions increase, the availability of ground-based resources will begin to strain, especially at the scale required for effective orbital debris removal and satellite servicing. Additionally, interplanetary exploration comes with its own challenges that come with dependence on ground-based resources, such as information lag-time. As a result, increased data analysis and decision-making capabilities for space-based autonomous systems is warranted.

A significant portion of increasing these capabilities lies with autonomous navigation and methods by which the spacecraft may build and modify its own trajectory based on information gathered in real-time. In scenarios where the spacecraft's operational environment may or may not be defined, the challenge of navigation starts as a simultaneous localization and mapping (SLAM) problem. The spacecraft must be able to understand what the operational environment looks like where it is within the operational environment. There has been an extensive amount of literature dedicated to solving the SLAM problem with ground-based applications and with ground-based resources. However, few have found utilization in the space domain.

Simultaneous Localization and Mapping in space presents its own challenges that makes the gathering and interpretation of information difficult. The rapidly changing lighting conditions cause low signal-to-noise ratios and high contrast images that render the traditional feature identification and tracking techniques near ineffective. Subsequently, the filtering techniques that rely on feature-identification tend to diverge and mischaracterize the pose of the spacecraft. These challenges have made autonomous space exploration and orbital debris difficult and overcoming these challenges through autonomous system

sensing and navigation development will help push scientific advancement and exploration of the solar system.

This work will decrease the knowledge gap presented by focusing on filter robustness to mis-identification errors by applying a new almost global asymptotic stable filter to the SLAM problem. Combining this with recently derived feature association-free processing methods, will drive autonomous sensing capabilities forward and adequately equip them for space applications. The technologies developed here can also be applied to aerial and ground-based systems that rely significantly on localization and mapping in unknown environments.

1.1. Autonomous Rendezvous, Proximity Operations, and Docking

While spacecraft maintain a relatively close proximity, such as seen in Figure 1.1, ground-based measurements are unable to accurately provide state estimates due to the relative proximity of the target and agent spacecraft. Known as the diffraction limit, this threshold at which target and agent spacecraft become near indistinguishable presents a significant hazard for operations relying solely on ground-based observations. This problem is magnified for interplanetary missions during which the communication lag time renders state estimates made via ground-based observations obsolete and impractical.

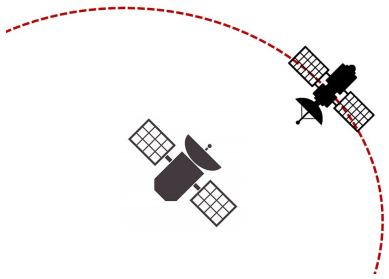

Figure 1.1 Example ARPOD scenario with one spacecraft (chaser) maintaining close proximity with another spacecraft (target).

Typically defined as two or more spacecraft maintaining relatively close distance and velocity, ARPOD scenarios have become a necessity for a significant portion of space

missions. Most applications of ARPOD are an attempt to reduce/remove the necessity for a human operator, increasing safety and decreasing cost. A large sum of these missions include on-orbit satellite servicing, space asset monitoring, and decision-making. In other scenarios, autonomy is unquestionably required. These types of missions include long duration interplanetary mission where communication lag-times become cumbersome and missions that inherently expose any man to harsh environments beyond which current technology can accommodate.

1.2. Problem Statement

The recent near-collision event between the two defunct IRAS and GGSE satellites has added fuel to the discussion for active orbital debris removal. Mark and Kamath in their paper entitled *Review of Active Space Debris Removal Methods* (2019) survey a number of satellite-based methods for active orbital debris removal, all of which require a high-degree of autonomy which can be aided by the improvement of relative optical navigation (OpNav) techniques OpNav has become state-of-the-art to augment ground-based radiometric measurements for precise satellite localization. However, there are situations, during RPO and interplanetary missions, that necessitate full reliance of on-board relative localization schemes.

1.2.1. Mission Hazards

In fact, technologies to mitigate this problem for orbital debris removal, on-orbit satellite servicing, have become of increasing interest to the defense, scientific, and commercial sectors. These technologies are under development to explicitly prevent near-conjunction and conjunction events that significantly increase the number of orbital debris which presents further hazards for already difficult space-operations. As seen by the Iridium 33-Cosmos 2251 collision in 2009 (Kelso et al., 2009).

A major hindrance to the success of these technologies have proven to be the navigation suite according to (C. Dennehy & Carpenter, 2006; C. J. Dennehy & Carpenter, 2011; Holland, 2002; Reesman & Rogers, 2018). A full overview of these and related problems will be given in Section 2.1.. Here, it is important to know that problems in the navigation

suite present mission-level hazards due to imprecise knowledge of state that influences flawed autonomous decision-making creating either a mission-failure or necessitating a significant level of human intervention.

In other cases, such as the Hayabusa 1, Hayabusa 2, and OSIRIS-REx missions (Barnouin et al., 2020; Yamaguchi et al., 2018; Yoshimitsu et al., 2009) the potential for human intervention, GPS, or other standard means of navigation may not be available. Creating a requirement for increased capabilities in relative navigation via visual methods.

To summarize, Reesman and Rogers in *Getting in Your Space: Learning from Past Rendezvous and Proximity Operations* (2018) state "A key issue with space-based navigation is that the precise state of the system is rarely, if ever, known perfectly…" (pg. 6).

1.2.2. Space Environment

Precise state knowledge is particularly challenging within the space environment due to adverse lighting conditions, coupled relative dynamics, and large scenario-scaling. Each of these contributors present different obstacles any state determination scheme must overcome to accurately estimate the spacecraft's relative position and velocity.

Lighting conditions pose a hazard particularly for vision-based sensors that rely on incoming light to view their environment. Consider an ARPOD scenario during which a chaser spacecraft is observing a target spacecraft, similar to the depiction in Figure 1.1. Depending on the location of the two spacecraft system to the sun, the lighting conditions may vary, see Figure 1.2. Particularly in low-earth orbit (LEO), the lighting conditions for optimal observations are minimal. Either the system will lie within the Earth's shadow and the chaser will have low to no visibility of the target, or the system will be at such an angle that the sun will lie within the camera's field-of-view (fov), effectively blinding the camera to everything else in its fov as seen in the image of the International Space Station (ISS) in Figure 1.3.

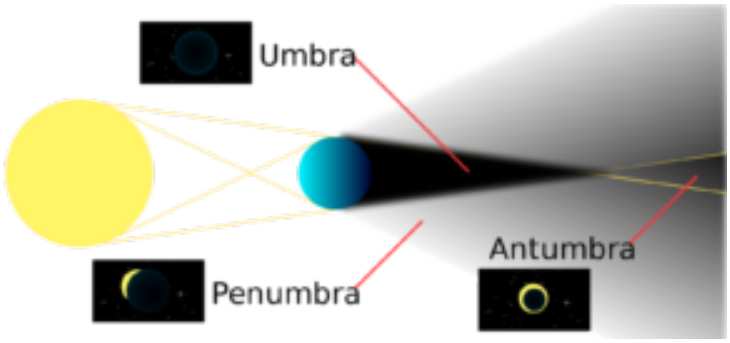

Figure 1.2 Parts of the Earth's shadow illustrating visibility of an observer viewing the sun located in each part. Image Credit: Umbra01 by Daniel M. Short CC BY-SA 2.5.

Figure 1.3 Example of on-orbit lighting conditions.

1.3. Autonomous Decision-Making

A key element of this research is improving the ability of autonomous systems to make the correct decision under a variety of influences. Particularly, this work focuses on guidance and navigation to answer the question: Where and how should an agent move given a set of information? This question becomes very important for space systems due to the Mission Hazards outlined in Section 1.2.1. Autonomous systems must be capable of making these decisions before they can be wholly relied upon for in-space applications.

1.3.1. Probability in Decision-Making

Particularly for guidance and navigation applications, this decision-making process is influenced by the probability a spacecraft occupies a state and whether or not that that state puts the spacecraft at risk of collision, or any other undesired occurrence. This probability

measure is dependent on the mean and uncertainty of the state, as shown in Equation 1.1.

$$F(x) = \int_{\mathcal{B}} \frac{1}{2\pi|P|^{\frac{1}{2}}} \exp(-\frac{1}{2}x^T P^{-1} x) \tag{1.1}$$

where P is the state covariance matrix, quantifying uncertainty defined by:

$$P \triangleq \mathbb{E}[(x - \hat{x})(x - \hat{x})^T] \tag{1.2}$$

with x being the true or mean state, and $\hat{x}$ is the estimated state. $F(x)$ is the probability that the spacecraft occupies that state.

This probability measure provides a quantification by which autonomous systems can make informed decisions on guidance and navigation. Note, that to provide an effective probability measure, an accurate mean and uncertainty parameters must be provided. An estimate is no good without a quantifying reliability measure, and a reliability measure is no good without a quantifying estimate. Both are necessary.

1.3.2. Contributors to State Uncertainty

The ability of the spacecraft to perform relative operations is susceptible to the deficiencies posed by the chosen relative sensing modality. Ground based observations such as radar and optical telescopes have higher relative uncertainties and problems distinguishing spacecraft when these spacecraft get too close to the diffraction limit. For this reason, this work employs on-board sensors such as the LiDAR and the visual camera to obtain relative state measurements. While these sensing modalities have their own associated uncertainties, they are significantly less than ground-based observations.

1.4. Camera Perception

Visual sensing has played a key role in the advancements of autonomous robotics here on Earth. The development of key situational awareness and collision avoidance technologies has laid the foundation for the autonomous driving industry, factory robotics, and unmanned aerial vehicles. The information provided by these visual sensing modalities allows the robot to make informed decisions based on its immediate surroundings.

Similarly, such techniques can be applied within the space domain. Fully autonomous algorithms can be used for rendezvous and proximity operations (RPO) and interplanetary exploration by providing the spacecraft with the information required to make knowledgeable decisions about the state of its environment.

1.4.1. Lighting Conditions

In many visual sensing applications, it is common to use feature-based approaches to obtain relative position measurements between a camera and its environment. This area of research has produced a number of different feature identification and association algorithms such as ORB ((Mur-Artal et al., 2015)), SURF ((Bay et al., 2006)), and SIFT ((Lindeberg, 2012)). However, particularly in the space environment, these feature-identification methods struggle to identify relevant information due to low signal-to-noise ratios, high contrast imaging, and rapidly changing lighting conditions.

Because of the lighting conditions discussed in Section 1.2.2., visual cameras may have trouble identifying and associating features across a series of images. As a result, erroneous features may be detected, missed, or misplaced. The inherent noise of this scheme must be overcome by a robust, stable state estimation capable of accounting for potentially high levels of noise from feature based measurement schemes.

1.4.2. Loss of Dimensionality

Additionally, cameras, specifically mono-cameras, have great difficuly measuring range. This effectively reduces a three-dimensional scene into a two-dimensional representation. By losing accuracy in the range dimension, may cause an ambiguity in relative orbit estimation, two different orbits look the same. This may cause the chaser spacecraft to incorrectly estimate its relative orbit to the target.

1.4.3. Computational Loads

Conducting the appropriate image processing to identify and associated features can be exceptionally expensive to perform real-time processing (Lovelly et al., 2018). This problem is magnified on space-grade processors that are typically single-threaded (not parallel) due to radiation shielding and mass constraints. As a result, a trade-off must occur.

Any solution must either choose to accurately estimate relative state information, or be computationally efficient to be performed in real-time.

1.5. Requirements for a Solution

At its core, this is a computer vision problem that has a solution through the lens of state estimation. To accommodate for the problems presented in space-based computer vision, any potential solution must accomplish three tasks:

- Accurately represent the system uncertainty
- Be robust to high-levels of measurement noise
- Compute estimates and uncertainties efficiently

This thesis presents the beginnings of an extended project to accomplish each of the above listed objectives. With the end goal of improving the overall efficacy of vision-based navigation methods for autonomous operations on-orbit and in interplanetary exploration. This thesis focuses on the first two objectives to lay a baseline for future work. Once the first two objectives are accomplished, computationally efficiency will be considered.

2. Literature Review

This chapter discusses previous literature that has laid a foundation for the development of this work. It expands on the stated problem by providing real-world examples of autonomous on-orbit operations and a brief description of their outcomes. Next, it discusses some of the current research aimed at developing solutions to these problems and to improve the current state-of-the-art in on-orbit navigation technology. Finally, this chapter provides the necessary theoretical background used in the development of this work.

2.1. Real World Examples

The government, scientific, and commercial sectors have demonstrated an increasing interest in on-orbit operations with a variety of objectives. Many of which have provided technical demonstrations for autonomous on-orbit capabilities that have resulted in off-nominal outcomes. This section presents real-world examples that demonstrate the necessity for improved autonomous decision-making and navigation filtering for effective on-orbit and interplanetary operations.

2.1.1. Satellite Servicing Examples

There have been a number of technology demonstrations to exhibit the capabilities of autonomous systems for on-orbit satellite servicing, and autonomous rendezvous. One of the first being DART (Demonstrate Autonomous Rendezvous Technology) of 2005. The intended goal of this mission was to autonomously rendezvous and perform proximity operations to an uncooperative target.

However, during the mission the spacecraft began to use additional amounts of fuel than what was required. In his report, (C. Dennehy & Carpenter, 2006) finds that this mishap was due to faulty estimates from the navigation filter. These faulty estimates were a result of divergence of the Extended Kalman Filter (EKF) that caused the spacecraft to believe it was at an incorrect state. A few years later Orbital Express, an on-orbit satellite servicing technical demonstration funded by DARPA (Defense Advanced Research Projects Agency), experienced navigation suite degradation that caused an underestimated its uncertainty

causing the chaser spacecraft to bump into the passive target spacecraft (C. J. Dennehy & Carpenter, 2011).

2.1.2. Asteroid Exploration

The Hayabusa 1, Hayabusa 2, and OSIRIS-REx missions have had significant amounts of ground-based operation for terrain mapping and relative state estimation (Barnouin et al., 2020; Yamaguchi et al., 2018; Yoshimitsu et al., 2009). In each, a team of scientists collected, processed, and evaluated terrain data to map the surface of the asteroid. Based on these evaluations, the landing site was selected and the spacecraft's trajectories were generated. However, as seen with Hayabusa 1, ground-based image processing and decision-making becomes inefficient as the spacecraft nears the surface of the asteroid. The rough terrain present on many asteroids leaves little margin for error during descent and landing magnifies the importance of accurate relative state estimation. As a part of NASA's Project Morpheus to develop vertical takeoff and vertical landing capabilities, the Autonomous Landing Hazard Avoidance Technology (ALHAT) (Ivanov et al., 2013) focused on equipment development for autonomous landings. ALHAT demonstrated advancements in terrain-relative navigation (TRN) and hazard detection and avoidance technologies. Presently, the Artemis program is employing these methods for autonomous landing.

2.2. Related Work

Research conducted by Setterfield (2017) utilizing the Synchronized Position Hold Engage and Reorient Experimental Satellites (SPHERES) for 3D mapping, relative pose estimation, and trajectory planning for spin stabilization mission used a factor graph methodology to build and navigate a relative map using a combination of stereo cameras, LiDAR, and intertial measurement units (IMUs). This work uses a feature identification approach with an EKF for mapping and localization and is subsequently vulnerable to mis-identification errors causing filter divergence.

A graph-based approach to space SLAM is discussed in (Nakath et al., 2019). By adaptively adjusting filter behavior for localization or mapping operations by weighting

information intake with a gain factor controlled by the uncertainty distribution, it improves scenario specific performance. Although, the work specifically discusses asteroid applications, the same methodology can be directly applied to relative orbital motion scenarios. It is mentioned that in the interest of numerical stability, the camera should only monitor the illuminated portions of the asteroid. As a result, the presented algorithm is limited in application. A probability hypothesis density (PHD) filter based method to perform in-space SLAM based in random-finite set theory is proposed in (Schlenker et al., 2019). However, because the pose estimation scheme remains as a particle filter, it is still susceptible to divergence.

In review, the methodologies presented showcase a variety of approaches for effective SLAM implementation in space. However, many attempt to tailor the representation of measurement data to reduce the probability of divergence rather than improve the stability of the filter directly. Therefore, each is inclined to divergence in the presence of incorrect data association. This work attempts to fill this knowledge gap by not relying on feature-based detection methods and focusing on filter stability for appropriate state estimation in the presence of mis-identification errors.

2.3. Work on the Lie Groups

The work on Lie Groups and the development of geometrically exact integrators on these smooth manifolds have allowed for significant advancement in modeling and simulation of dynamic systems. Lie Groups are a general area of mathematics developed by Sophus Lie that have found significant uses in topology, dynamic systems theory, and more recently, state estimation for robotics systems.

2.3.1. Lie Group Variational Integration

Focusing on spacecraft activities inherently poses a 12 degree-of-freedom dynamics problem that is dependent on the parameters of the target spacecraft. This problem is magnified in the presence of highly-perturbed gravitational fields, such as the ones found about asteroids. The commonly assumed point-mass body becomes insufficient due to the torques gravity exerts on a rigid body. At a kinetic level, the rotational and translational

motion of the spacecraft are tightly coupled in the orbital regime, and decoupling each facet of motion inherently introduces modeling errors. For this reason, the work chooses to work on the Special Euclidean Group ($SE(3)$) - a specific variation of a Lie Group. Integrating the dynamics directly on $SE(3)$ couples the motion in a compact form allowing for higher-fidelity modeling without significantly increasing computational time (Lee et al., 2007). Propagating the dynamics in this way maintains the added benefit of preserving the geometric characteristics of the system allowing for a greater level of accuracy for extended periods of time.

Over the past decade a series of works (Lee et al., 2007; Lee & Leve, 2014; Nordkvist & Sanyal, 2010) have been published on the theory, development, and applications of a Lie Group Variational Integrator (LGVI) that preserved the geometric characteristics and allows for higher-fidelity coupled dynamics modeling. The LGVI has a number of desirable qualities that make it attractive for propagating dynamics. The LGVI is a class of geometric integrators that are geometric characteristic preserving (Leok, 2007). This property alone makes this class of integrators allow for accurate solutions for longer periods of time than other methods - such as Runge-Kutta algorithms. By evolving directly on the smooth manifolds on which they exist they mitigate any reliance on reprojections, constraints or local coordinates that reduced the efficacty of other algorithms. For this reason they are a basis for efficient exact algorithms.

2.3.2. Lie Group Variational Filtering

Building off this work, Izadi and Sanyal develop a Lie Group Variational Filter (LGVF) (Izadi et al., 2015; Izadi & Sanyal, 2016; Sanyal, Izadi, & Butcher, 2014; Sanyal, Izadi, Scheeres, et al., 2014) that is shown to use strictly vector measurements to accurately estimate the pose of a body. The developed filtering scheme is model agnostic and is almost globally asymptotically stable under no measurement noise and bounded stability under measurement noise. However, a method to quantify uncertainty using this method was not developed. This allows for autonomous systems to estimate its state without relying on external measurement sources such as GPS, which may not be available for all on-orbit and

interplanetary missions. As such, the filter lays the foundation on which these thesis expands on to include a method of uncertainty measurement.

2.4. Lie Group Theory

In recent years, the robotics community has seen an increasing trend in the applications of Lie Groups for estimation. Specifically, they become useful in representing pose for SLAM and visual odometry applications. The authors recognize the abstraction of Lie theory and have provided this section as a brief introduction to its applications in state estimation. For a more detailed discussion on Lie theory as is pertains to state estimation, the authors point the interested reader to (Sola et al., 2018) which provides a thorough introduction to Lie theory for roboticists.

2.4.1. The Lie Group

Specifically, a Lie Group is a smooth manifold that upholds the criteria of a group.

1. Closure: $g \circ h \in \mathcal{G}$
2. Identity: $e \circ g = g \circ e = g$
3. Inverse: $g^{-1} \circ g = e$
4. Associativity: $(g \circ h) \circ f = g \circ (h \circ f)$

where $\mathcal{G}$ is defined to be a group, $\circ$ is an operator on that group, and g, h, $f \in \mathcal{G}$. Closure under operation '$\circ$', defined mathematically above, states that if two operands reside in a group the resulting quantity through that operation will also reside in that group. The Identity of a group applied to a member of that group will result in the same member of that group. The Inverse of a group applied to a member of that group will result in the Identity of that group. Associativity states that the same result can be obtained through different groupings of the same order of the operands.

Mathematically, a smooth manifold is an infinitely differentiable manifold, or the smooth manifold has infinitely many continuous derivatives; that is to say a smooth manifold is a surface that exhibits no corners, peaks, or sharp turns. The fact the manifold is smooth indicates the existence of a tangent vector space at each point along the smooth manifold.

Some common examples of Lie Groups in dynamic systems theory are the rotation matrix $\mathbf{R} \in \mathrm{SO}(n)$ which is the Special Orthogonal Group, the unit quaternion $q \in S^3$ which is the symmetric group of the third degree, and the pose matrix $\mathbf{G} \in \mathrm{SE}(n)$ which is the Special Euclidean Group where $\mathbf{r} \in \mathbb{R}^n$, and $\mathbf{0} \in (\mathbb{R}^n)^T$:

$$\mathbf{G} = \begin{bmatrix} \mathbf{R} & \mathbf{r} \\ \mathbf{0} & 1 \end{bmatrix} \tag{2.1}$$

2.4.2. The Lie Algebra

The first tangent space of the Lie Group is often referred to as its Lie algebra which is expressed as $\mathfrak{m} \triangleq T_{\varepsilon}\mathcal{M}$ at the identity and as $\mathfrak{m} \triangleq T_{\boldsymbol{\chi}}\mathcal{M}$ at every other point in the group - $\mathcal{M}$ is a smooth manifold and $\boldsymbol{\chi}$ is a specific point on that manifold. While the structure of the Lie group prevents typical calculus, the tangent space, that can be represented as a vector space, this attribute conveniently allows for an alternative representation of the Lie group on which calculus may be performed. Figure 2.1 provides a visual representation of a smooth manifold and its tangent space.

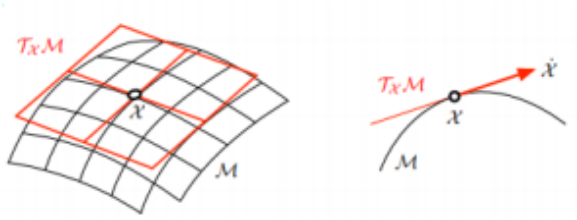

Figure 2.1 A smooth manifold and its tangent space (Sola et al., 2018).

Every element of the Lie algebra $\mathfrak{m}$ with m degrees of freedom can be expressed in $\mathbb{R}^m$. Conveniently the degrees of freedom of $\mathfrak{m}$ is equal to the number of degrees of freedom in $\mathcal{M}$. This idea can be directly applied in dynamic systems theory. For example, take a point $\boldsymbol{\chi}$ evolving on a smooth manifold. Physically, this may be taken to represent the pose of a rigid body. The tangent space of the manifold can then be interpreted as its velocities $\dot{\boldsymbol{\chi}} = \delta\boldsymbol{\chi}/\delta t$.

2.4.3. Fundamental Operations

To fully understand Lie Group Theory, this section defines a few fundamental operations available to make use of Lie Group Theory for dynamical systems. Each of the operations have been fundamental to the development of Lie Group Theory as applied to dynamic systems. Each of these operations provide the means an element of a Lie group may be transformed to an element of its Lie algebra (and vice versa), an element may undergo a frame transformation, and how dynamic systems theory may be directly applied.

2.4.3.1. Topographical Mappings

Because the transformation from a Lie algebra to its vector space representation is a common operation, the $(\cdot)^\wedge$ and its inverse, $(\cdot)^\vee$ are defined:

$$\begin{aligned} (\cdot)^\wedge &: \mathbb{R}^m \to \mathfrak{m} \\ (\cdot)^\vee &: \mathfrak{m} \to \mathbb{R}^m \end{aligned} \tag{2.2}$$

These topographical mappings allow for efficient transformation between the two spaces. It must be noted that these become an overloaded operator depending on the dimensionality of the space. Here, the topographical mappings for $\mathfrak{so}(3)$ and $\mathfrak{se}(3)$ are defined. The author chooses to use $(\cdot)^\times$ as the operator to perform this mapping for $\mathfrak{so}(3)$, the Lie algebra of $\mathrm{SO}(3)$, and $(\cdot)^\wedge$ as the operator to perform this mapping for $\mathfrak{se}(3)$, the Lie algebra of $\mathrm{SE}(3)$:

$$\boldsymbol{\omega}^\times = \begin{bmatrix} 0 & -\omega_3 & \omega_2 \\ \omega_3 & 0 & -\omega_1 \\ -\omega_2 & \omega_1 & 0 \end{bmatrix} \tag{2.3}$$

$$\mathbf{V}^\wedge = \begin{bmatrix} \boldsymbol{\omega}^\times & \boldsymbol{\nu} \\ \mathbf{0} & 0 \end{bmatrix} \tag{2.4}$$

where $\mathbf{V} = [\boldsymbol{\omega}^T \ \boldsymbol{\nu}^T]^T$. The inverses of these mappings are denoted $(\cdot)^|$ and $(\cdot)^\vee$ for $\mathfrak{so}(3)$ and $\mathfrak{se}(3)$, respectively.

2.4.3.2. The Adjoint Map

In dynamic systems theory it is often necessary to define multiple frames to establish a relationship between each body of interest, and a global representation of the scenario as a whole. This necessitates a means to transform from a local frame to a global frame. The adjoint and the adjoint matrix provides such a means to accomplish this transformation.

$$ {}^{\varepsilon}\boldsymbol{\tau}^{\wedge} = \mathrm{Ad}_{\boldsymbol{\chi}}({}^{\chi}\boldsymbol{\tau}^{\wedge}) = \boldsymbol{\chi}\,{}^{\chi}\boldsymbol{\tau}^{\wedge}\boldsymbol{\chi}^{-1} \tag{2.5} $$

where ${}^{\chi}\boldsymbol{\tau}^{\wedge}$ is a Lie algebra defined in $\mathfrak{m}$ with respect to the local frame χ. ${}^{\varepsilon}\boldsymbol{\tau}^{\wedge}$ is that same Lie algebra expressed in the global frame established at ε. Therefore, $\mathrm{Ad}_{\boldsymbol{\chi}} : \mathfrak{m} \to \mathfrak{m}$.

$$ \begin{aligned} \text{Linearity} &: \mathrm{Ad}_{\boldsymbol{\chi}}(a\boldsymbol{\tau}^{\wedge} + b\boldsymbol{\gamma}^{\wedge}) = a\mathrm{Ad}_{\boldsymbol{\chi}}(\boldsymbol{\tau}^{\wedge}) + b\mathrm{Ad}_{\boldsymbol{\chi}}(\boldsymbol{\gamma}^{\wedge}) \\ \text{Homomorphic} &: \mathrm{Ad}_{\boldsymbol{\chi}}(\mathrm{Ad}_{\boldsymbol{\Psi}}(\boldsymbol{\tau}^{\wedge})) = \mathrm{Ad}_{\boldsymbol{\chi}\boldsymbol{\Psi}}(\boldsymbol{\tau}^{\wedge}) \end{aligned} \tag{2.6} $$

Due to the linearity and homomorphic properties, noted in Equation 2.6 of the $\mathrm{Ad}_{\boldsymbol{\chi}}$ operator, it is classified as a linear operator and therefore, an analogous matrix operator may be defined that $\mathbf{Ad}_{\boldsymbol{\chi}} : \mathbb{R}^m \to \mathbb{R}^m$

$$ \mathbf{Ad}_{\boldsymbol{\chi}} = (\boldsymbol{\chi}\,{}^{\chi}\boldsymbol{\tau}^{\wedge}\boldsymbol{\chi}^{-1})^{\vee} \tag{2.7} $$

This work focuses on two primary Lie groups $SO(3)$ and $SE(3)$. For $SO(3)$, $\mathbf{Ad}_{\boldsymbol{\chi}} = \mathbf{R}$ is the standard rotation matrix. The $\mathbf{Ad}_{\boldsymbol{\chi}}$ for $SE(3)$ takes the form:

$$ \mathbf{Ad}_{\mathbf{T}} = \begin{bmatrix} \mathbf{R} & \mathbf{b}^{\times}\mathbf{R} \\ \mathbf{0} & \mathbf{R} \end{bmatrix} \in \mathbb{R}^{6\times 6} \tag{2.8} $$

where,

$$ \mathbf{T} = \begin{bmatrix} \mathbf{R} & \mathbf{b} \\ \mathbf{0} & 1 \end{bmatrix} \tag{2.9} $$

This allows for a linear transformation of the vector elements of the Lie algebra at $\mathbf{T}$ to the origin ${}^{\varepsilon}\mathbf{V}^{\wedge} = \mathbf{Ad}_{\mathbf{T}}^{\mathbf{T}}\mathbf{V}^{\wedge}$. Analogously, the adjoint mapping can be defined to manipulate elements of $\mathfrak{m}$. The adjoint matrix operator for elements of $\mathfrak{se}(3)$ is defined as:

$$\mathbf{ad}_{\mathbf{V}} = \begin{bmatrix} \boldsymbol{\omega}^{\times} & \mathbf{0} \\ \boldsymbol{\nu}^{\times} & \boldsymbol{\omega}^{\times} \end{bmatrix} \tag{2.10}$$

This mapping becomes significant for the linear transformation of vector elements in the second tangent space of the manifold. In dynamic systems, that is acceleration.

2.4.3.3. Exponential and Logarithmic Maps

The relationship between the Lie group and its Lie algebra is tied through the exponential map. Given a dynamic system that takes the form:

$$\dot{\mathbf{T}} = \mathbf{T}\mathbf{V}^{\wedge} \tag{2.11}$$

The solution of this differential equation is of the standard form:

$$\mathbf{T}(t) = \mathbf{T}(0)\exp(\mathbf{V}^{\wedge}t) \tag{2.12}$$

Geometrically, the mapping curves the tangent vector to form on the smooth manifold $\exp(\cdot) : \mathfrak{m} \to \mathcal{M}$. Figure 2.2 shows a visualization of this mapping.

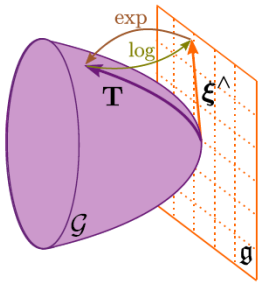

Figure 2.2 Visualization of the exponential and logarithmic mapping of a smooth manifold and its tangent space (Mangelson et al., 2020).

Because $\mathbf{T}(t)$, $\mathbf{T}(0) \in SE(3)$, by closure, $\exp(\mathbf{V}^{\wedge}t)$ must exist in $SE(3)$. It is computationally convenient to represent the exponential map as a closed form solution that may be derived via its Taylor Series Expansion:

$$\exp(\mathbf{V}^{\wedge}t) = \sum_{n=0}^{\infty} \frac{1}{n!}(\mathbf{V}^{\wedge}t)^n \tag{2.13}$$

which, through expansion and some algebraic manipulation can be presented in closed-form as:

$$\exp(\mathbf{V}^{\wedge}t) = \begin{bmatrix} \mathbf{R} & \mathbf{S}p \\ \mathbf{0} & 0 \end{bmatrix} \tag{2.14}$$

where,

$$\mathbf{R} = I + \sin(\theta)\hat{e}^{\times} + (1 - \cos(\theta))\hat{e}^{\times 2} \in SO(3) \tag{2.15}$$

θ and $\hat{e}$ are the principal angle and axes determined from $\boldsymbol{\omega}^{\times}t$ implicit in $\mathbf{V}^{\wedge}t$, and where,

$$\mathbf{S} = I + S_1\hat{e}^{\times} + S_2(\hat{e}^{\times})^2 \tag{2.16}$$

with,

$$S_1 = \frac{1 - \cos\theta}{\theta} \tag{2.17}$$

$$S_2 = \frac{\theta - \sin\theta}{\theta} \tag{2.18}$$

This representation of S_1 and S_2 are obtained via algebraic manipulation of the Taylor Expansion, mentioned previously, to construct the Taylor Series form of $\cos\theta$ and $\sin\theta$ with the additional terms included. Therefore, Equations 2.15 and 2.16 present a closed-form solution of the exponential map.

The inverse of the exponential map is the logarithmic map and takes elements of the manifold back onto its tangent space $\log(\cdot) : \mathcal{M} \rightarrow \mathfrak{m}$. Specifically for $\mathbf{T} \in SE(3)$:

$$\log(\mathbf{T}) = \begin{bmatrix} \Theta^{\times} & \mathbf{S}^{-1}b \\ \mathbf{0} & 0 \end{bmatrix} \tag{2.19}$$

where Θ is obtained from $\mathbf{R}$:

$$\Theta^{\times} = \frac{\phi}{2\sin(\phi)}(\mathbf{R} - \mathbf{R}^{T}) \tag{2.20}$$

where $\phi = \cos^{-1}(0.5 \text{ tr}(\mathbf{R}) - 0.5)$.

2.5. Probability and Uncertainty

In order to thoroughly understand estimation, a clear understanding of probability and uncertainty must be built. As mentioned in Chapter 1, perfect state knowledge is impossible to achieve. For this reason, probability and uncertainty metrics are commonplace in guidance and navigation.

2.5.1. The Gaussian Distribution

The Gaussian distribution, also known as the normal distribution, is a specific type of continuous probability distribution. It is commonly used within estimation theory to model noise. Measurements may be sampled from a Gaussian distribution to provide perturbations to the measurements that are representative of the uncertainties.

The Gaussian distribution is characterized as having an area under its curve equal to one and a symmetry about the mean values as can be seen in Figure 2.3. The mean value, μ, and the standard deviation, σ, are all that is needed to find the probability a particular sample is obtained. The quantity σ^2 is known as the variance and is frequently used in estimation theory to represent the uncertainty in a mean estimate.

Because of these characteristics it allows for simplifications in the theoretical developments of many concepts in stochastic estimation and control theory. Modeling and

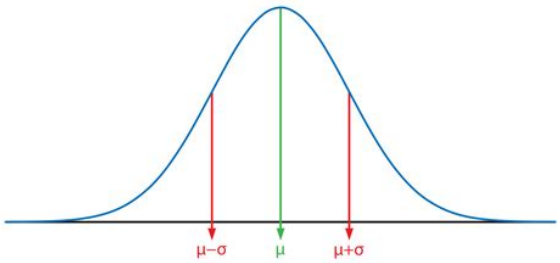

Figure 2.3 A sample Gaussian Distribution.

applying non-Gaussian distributions to these same concepts is still an active area of research.

2.5.2. Uncertainty Representation in Lie Group Theory

Uncertainty cannot be explicitly represented on the Lie group. Rather uncertainty is represented on the tangent space of the Lie group known as the Lie algebra. This Lie algebra is a vector space on which calculus is allowed to be performed. For the Special Euclidean group this can be notated as $\mathrm{SE}(3)$ and $\mathfrak{se}(3)$, respectively Setting $\tilde{\mathbf{T}} \in \mathrm{SE}(3)$ and $\boldsymbol{\xi} \in \mathbb{R}^6 \sim \mathcal{N}(0, \boldsymbol{\Sigma})$ is a Gaussian-noise process with $\boldsymbol{\Sigma} = \mathrm{E}[\boldsymbol{\xi}\boldsymbol{\xi}^T]$. $\tilde{\mathbf{T}}$ can then be perturbed such that:

$$\mathbf{T} = \tilde{\mathbf{T}} \exp\left(\boldsymbol{\xi}^{\wedge}\right) \tag{2.21}$$

The value $\mathbf{T}$ is a perturbed quantity obtained from the mean $\tilde{\mathbf{T}}$ governed by a perturbation $\boldsymbol{\xi}$ sampled from a Gaussian noise process. Conceptually, a vector is mapped to the Lie algebra and then mapped onto the Lie Group to apply a perturbation to a quantity on the Lie Group.

3. Special Euclidean Group Filter Derivation

This chapter details the derivation of a variational filter founded in the Special Euclidean Group, $SE(3)$. This development follows the procedure firtst developed by Izadi (2016). For clarification, this derivation is repeated here and to ensure the implementation of this filter is understood before uncertainty representation is included in later chapters.

3.1. Measurement Model

Take a scenario where an agent is monitoring a target from a relative trajectory. A visual of this system is provided in Figure 3.1. The remainder of this section details how each of these vectors are measured and will be used throughout the chapter to developed the LGVF.

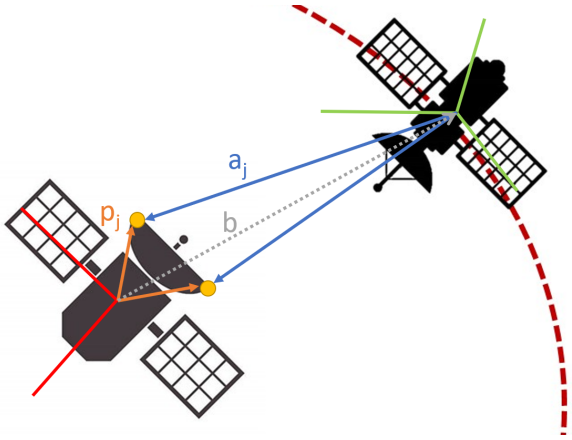

Figure 3.1 Measurement model with vector measurements to identifiable features on target body. This is used for derivation of the Lie Group Variational Filter.

3.1.1. Position Measurement Model

Assign Frame O in the figure to be an Inertial Frame, and Frame S to be the body-fixed frame of the chaser. The rotation matrix $\mathbf{R}$ maps vectors expressed in S to O. Because only one sensor is considered, the notation $(\cdot)^k$ is omitted. Now, take $\mathbf{q}_j$ to be the measurement vector of feature j expressed in S. This same feature is expressed as $\mathbf{p}_j$ on O. The true position of S on O is the vector $\mathbf{b}$, and the sensor placement relative to S is $\mathbf{s}$.

Mathematically, and without any measurement noise, these vectors are related through Equation 3.1

$$\mathbf{p}_j = \mathbf{R}(\mathbf{q}_j + \mathbf{s}) + \mathbf{b} = \mathbf{R}\mathbf{a}_j + \mathbf{b} \tag{3.1}$$

where $\mathbf{a}_j$ is the vector between feature j and the origin of S. To focus on the development of the measurement scheme and associated filters, and for notational convenience, it is assumed that the sensor is placed at the origin of S and therefore $\mathbf{q}_j = \mathbf{a}_j$.

While this form presents a convenient way to express the measurement vectors, a problem arises for the vectors expressed in the inertial frame because the exact position of the Inertial frame is rarely, if ever, known. Therefore, one strategy is to arbitrarily assign the origin of the inertial frame to be one of the features measured during the initialized timestep (t_0, $j = 0$). The orientation of this frame is assigned the same orientation as S so that the relative rotation $\mathbf{R}_0 = I_{3\times3}$. Now each of the features expressed in the inertial frame must be converted to the origin of the new inertial frame: $\mathbf{d}_j = \mathbf{p}_i - \mathbf{p}_0$ where $i = 1, 2..., n$ where n is the number of measured features. Similarly, $\mathbf{l}_j = \mathbf{a}_i - \mathbf{a}_0$ where $i = 1, 2, ..., n$.

The relationship between $\mathbf{d}_j$ and $\mathbf{l}_j$ is $\mathbf{d}_j = \mathbf{R}\mathbf{l}_j$ which can be written in matrix form as $D = RL$, where $D, L \in \mathbb{R}^{3\times n}$, $D = [0, d_1, d_2, ..., d_{n-1}]$ and $L = [l_0, l_1, ..., l_{n-1}]$. L can be thought of as the feature map expressed in S, and D is the feature map expressed in O, these vectors can now be used to estimate the pose of the chaser relative to target. In this case, the orientation of the chaser is not directly measured. Rather, it is obtained by solving Wahba's Cost function of the general form:

$$\mathcal{U}^0 = \frac{1}{2}\sum_{i=1}^{k} w_i(e_i - \hat{R}u_i)^T(e_i - \hat{R}u_i) \tag{3.2}$$

Specifically, how this is handled will be discussed in Section 3.2.

3.1.2. Velocity Measurement Model

For full state estimation, relative velocities must be taken into account. In this work, it is assumed the relative velocities of each of the features measured above are able to be measured. Because of the rigid body kinematics it is necessary for the velocities to be known or estimated: $\dot{\mathbf{\Omega}} = \mathbf{R}\mathbf{\Omega}^{\times}$ and $\dot{\mathbf{b}} = \mathbf{R}\boldsymbol{\nu}$ leads to the rigid body kinematic formulation $\dot{\mathbf{T}} = \mathbf{T}\mathbf{V}^{\wedge}$.

3.2. Filter Derivation

This next section provides the derivation of a filter founded using the Lagrange-d'Alambert Principle from Variational Mechanics onto the Special Euclidean group. This filter is found in (Izadi & Sanyal, 2016) to be have almost-global asymptotic stability to the origin, for error dynamics, using strictly vector measurements.

3.2.1. Error Dynamics

First, the pose and velocity estimation parameters are defined under the hat notation $\hat{(\cdot)}$:

$$\dot{\hat{\mathbf{T}}} = \hat{\mathbf{T}}\hat{\mathbf{V}}^{\wedge} \tag{3.3}$$

this allows for the estimation error to be defined:

$$\mathbf{h} = \mathbf{T}\hat{\mathbf{T}}^{-1} = \begin{bmatrix} \mathbf{Q} & \mathbf{b}^m - \mathbf{Q}\hat{\mathbf{b}} \\ \mathbf{0} & 1 \end{bmatrix} \in SE(3) \tag{3.4}$$

where $\mathbf{Q} = \mathbf{R}\hat{\mathbf{R}}^T$ is the attitude estimation error. From here, the error kinematics are defined to be:

$$\dot{\mathbf{h}} = \mathbf{h}\boldsymbol{\varphi}^{\wedge} \tag{3.5}$$

where $\boldsymbol{\varphi}$ is the velocity error $[(\boldsymbol{\omega}^m - \hat{\boldsymbol{\omega}})^T, (\boldsymbol{\nu}^m - \hat{\boldsymbol{\nu}})^T]^T$. In the case of perfect measurements, $x^m = x$. In the case of measurement noise, $x^m = x + \gamma$, where γ is a random perturbation governed by a Weiner Process. This inherently implies that the state estimates will try to converge to the measured values. This is under the assumption that there is no bias is the state measurements.

3.2.2. Error Lagrangian

Now that the error kinematics have been defined, it is possible to begin the derivation of the state estimation scheme founded in $SE(3)$. The goal now, is to develop a method that drives the error to the origin. Which, in this case, is $I_{4\times4}$. It is important to note that the smooth manifold on which rigid body motion exists ($SE(3)$, is comprised of translational

and rotational components. Here, in an effort to facilitate development, consider potential energy-like functions for the translational and rotational components. The rotational portion is considered as Wahba's Cost function a slight reformulation on Equation 3.2.

$$\mathcal{U}_r^0 = \frac{1}{2}(\mathbf{D} - \hat{\mathbf{R}}\mathbf{L})^T W (\mathbf{D} - \hat{\mathbf{R}}\mathbf{L}) \tag{3.6}$$

where W is a positive definite diagonal weighting matrix. The translational potential function is defined as:

$$\mathcal{U}_t^0 = \frac{1}{2}\kappa \mathbf{y}^T \mathbf{y} \tag{3.7}$$

where $\mathbf{y} = \bar{\mathbf{p}} - \hat{\mathbf{R}}\bar{\mathbf{a}}^m - \hat{\mathbf{b}}$.

The total potential energy function is then the sum of the rotational and translational potential energy functions:

$$\mathcal{U} = \mathcal{U}_r + \mathcal{U}_t \tag{3.8}$$

To obtain this formulation, an operator must be defined to map $\mathcal{U}_r^0 \in \mathbb{R}^{n\times n} \rightarrow \mathbb{R}^1$. This operator will be defined as $\Phi(\cdot) : \mathbb{R}^{n\times n} \rightarrow \mathbb{R}^1$. Φ itself must be a C^2-function that satisfies: $\Phi(0) = 0$ and $0 < \Phi'(\cdot) \leq \alpha(\cdot)$. With $\alpha(\cdot)$ is a Class - κ function. In this case, $\Phi(\mathcal{U}_r^0) = \mathcal{U}_r^0$ which leaves $\Phi'(\mathcal{U}_r^0) = I$. Alternatively, the kinetic energies are defined as:

$$\mathcal{T}_t = \frac{1}{2}\boldsymbol{\nu}^T M \boldsymbol{\nu} \tag{3.9}$$

$$\mathcal{T}_r = \frac{1}{2}\boldsymbol{\omega}^T J \boldsymbol{\omega} \tag{3.10}$$

which can be combined to form:

$$\mathcal{T} = \frac{1}{2}\boldsymbol{\varphi}^T \mathbb{J} \boldsymbol{\varphi} \tag{3.11}$$

where $\mathbb{J}$ is an artificial inertia-like kernel matrix used to help drive the estimates to their correct values. Now that the potential and kinetic energies of the errors have been defined, the error Lagrangian is defined as:

$$\mathcal{L} = \mathcal{T} - \mathcal{U} \tag{3.12}$$

plugging in values for $\mathcal{T}$ and $\mathcal{U}$:

$$\mathcal{L} = \frac{1}{2}\boldsymbol{\varphi}^T \mathbb{J}\boldsymbol{\varphi} - \frac{1}{2}(\mathbf{D} - \hat{\mathbf{R}}\mathbf{L})^T W(\mathbf{D} - \hat{\mathbf{R}}\mathbf{L}) - \frac{1}{2}\kappa \mathbf{y}^T \mathbf{y} \tag{3.13}$$

3.2.3. The Action Functional

The construction of the error Lagrangian leads to the formulation of an action functional:

$$\mathcal{S}(\mathcal{L}) = \int_{t_0}^{T} \mathcal{L} dt \tag{3.14}$$

Here, the Lagrange-d'Alembert Principle from variational mechanics is applied to Equation 3.15:

$$\delta\mathcal{S} = \delta \int_{t_0}^{T} \mathcal{L} dt = 0 \tag{3.15}$$

By plugging the Lagrangian of Equation 3.13 into Equation 3.15 and applying the variational operator (δ), the full nonlinear variational estimator for pose and velocities is obtained:

$$\mathbb{J}\dot{\varphi} = \mathbf{ad}_{\varphi}^T - Z - \mathbb{D}\varphi \tag{3.16}$$

$$\hat{\mathbf{V}} = \mathbf{V}^m - \mathbf{Ad}_{\mathbf{T}^{-1}}\varphi \tag{3.17}$$

$$\dot{\hat{\mathbf{T}}} = \hat{\mathbf{T}}\hat{\mathbf{V}}^{\wedge} \tag{3.18}$$

where $\mathbb{D}$ is a linear Rayleigh dissipation term, and

$$Z = \begin{bmatrix} \Phi'(\mathcal{U}_r^0) S_\Gamma + \kappa \bar{\mathbf{p}}^{\times} \mathbf{y} \\ \kappa \mathbf{y} \end{bmatrix} \tag{3.19}$$

with $\Phi'(\mathcal{U}_r^0) = I$. The above LGVF can be discretized for computer implementation as:

$$\Delta t (J\boldsymbol{\omega}_i)^{\times} = F_i \mathcal{J} - \mathcal{J} F_i^T \tag{3.20}$$

$$(M + \Delta t\mathbb{D}_t)\boldsymbol{\nu}_{i+1} = F_i^T M\boldsymbol{\nu}_i + \Delta t\kappa(\hat{\mathbf{b}}_{i+1} + \hat{\mathbf{R}}_{i+1}\bar{\mathbf{a}}_{i+1} - \bar{\mathbf{p}}_{i+1}) \tag{3.21}$$

$$\begin{aligned}(J + \Delta t\mathbb{D}_r)\boldsymbol{\omega}_{i+1} =& F_i^T J\boldsymbol{\omega}_i + \Delta t M\boldsymbol{\nu}_{i+1} \times \boldsymbol{\nu}_{i+1} \\ &+ \Delta t\kappa(\hat{\mathbf{b}}_{i+1} + \hat{\mathbf{R}}_{i+1}\bar{\mathbf{a}}_{i+1}) - \Delta t\Phi'(\mathcal{U}_r^0)S_{\Gamma_{i+1}}\end{aligned} \tag{3.22}$$

$$\hat{\mathbf{V}}_i = \hat{\mathbf{V}}_i^m - \mathbf{Ad}_{\hat{\mathbf{T}}_i^{-1}}\boldsymbol{\varphi}_i \tag{3.23}$$

$$\hat{\mathbf{T}}_{i+1} = \hat{\mathbf{T}}_i \exp\left(\Delta t\hat{\mathbf{V}}_i^\vee\right) \tag{3.24}$$

The full solution to Equation 3.15 and the subsequent discretization is left to (Izadi & Sanyal, 2016). However, the remaining significant undefined terms are defined here: F_i is a discretized rotation element, $\mathcal{J}$ is an inertia-like matrix found in the derivation of the discretized equations: $\mathcal{J} = \frac{1}{2}\text{tr}(J)I - J$. The Rayleigh Dissipation terms $\mathbb{D}_t$ and $\mathbb{D}_r$ are included to facilitate the dissipation of the "energy" leftover in the measurement residual. This allows for them to collapse towards the origin. S_Γ is another term found in the solution of Equation 3.15:

$$S_\Gamma = (DWL^{mT}\hat{\mathbf{R}}^T - \hat{\mathbf{R}}L^mWD^T) \tag{3.25}$$

It is noteworthy that in its current form Equation 3.20 is implicit and must be solved via a Newton-Rhapson method in (Nordkvist & Sanyal, 2010) or an explicit method presented in (Cardoso & Leite, 2003).

3.3. A Sample Scenario

This section describes a sample scenario of a relative orbital motion scenario that will be used through the rest of the work. Let us assume a chaser spacecraft follows an elliptical natural motion trajectory around a target spacecraft in a circular orbit about the earth described by the Clohessy-Wiltshire Dynamics in Equations 3.26.

$$\dot{\mathbf{x}} = \mathbf{A}\mathbf{x} \tag{3.26}$$

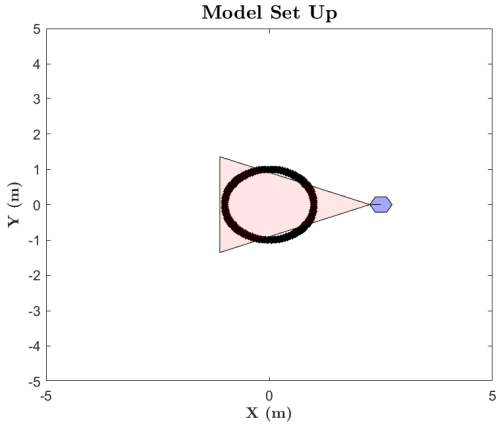

Figure 3.2 Representative model scenario with a "nadir" pointing spacecraft represented as the blue hexagon. Each $\times$ represents an identifiable feature on the target.

where $\mathbf{x}$, and $\dot{\mathbf{x}}$ are the translational states, and time derivative of the translational states, respectively and $\mathbf{A}$ is defined by Equation 3.27.

$$\mathbf{A} = \begin{bmatrix} 0 & 0 & 0 & 1 & 0 & 0 \\ 0 & 0 & 0 & 0 & 1 & 0 \\ 0 & 0 & 0 & 0 & 0 & 1 \\ 3n^2 & 0 & 0 & 0 & 2n & 0 \\ 0 & 0 & 0 & -2n & 0 & 0 \\ 0 & 0 & -n^2 & 0 & 0 & 0 \end{bmatrix} \tag{3.27}$$

where n is the mean motion of the target spacecraft. For simplicity it is assumed the spacecraft has an angular rate ($\boldsymbol{\omega}$) that maintains the alignment of the sensor boresight with the origin of the inertial frame:

$$\boldsymbol{\omega} = \frac{\mathbf{r} \times \dot{\mathbf{r}}}{r^2} \tag{3.28}$$

This is similar to a nadir pointing spacecraft. A representative scenario can be seen in Figure 3.2.

The relative attitude dynamics of the system are expressed via the kinematic differential equation for rotation matrices:

$$\dot{\mathbf{R}} = \mathbf{R}\boldsymbol{\omega}^{\times} \tag{3.29}$$

where $\boldsymbol{\omega}^{\times}$ denotes the skew symmetric mapping of the angular rate shown in Equation 2.3

Depicted in Figure 3.1 is a spacecraft following an elliptical natural motion trajectory equipped with a sensor capable of measuring feature position in the spacecraft's body fixed frame, denoted $\mathcal{S}$. An inertial frame is assigned to the center-of-mass of the target spacecraft and is denoted as frame $\mathcal{O}$. Then let rotation matrix $\mathbf{R}$ and translational vector $\mathbf{b}$ provide a relative pose transformation from frame $\mathcal{O}$ to frame $\mathcal{S}$.

3.4. Numerical Simulations of Mean Estimator

In order to maintain consistency throughout the work, a sample scenario was defined to verify performance of the estimator. All values are defined relative to the inertial/global frame defined at the center-of-mass of the target. The vehicular mass and moment of inertia were set to be $m = 0.42kg$ and $J = diag([0.0512, 0.0602, 0.0596])kg \cdot m^2$, respectively. The initial relative configuration was defined as: $\mathbf{b} = [2.5, 0, 0]^T$ and $\mathbf{R}_0 = \exp([0, 0, \pi]^T)$, and the initial velocities were set as $\boldsymbol{\nu}_0 = [0, 0.5, 0]^T$ and $\boldsymbol{\omega}$ defined by Equation 3.28.

The estimator also requires a set of initial values as initial conditions to begin. While, it does not matter where these values are set, the initial estimated states and gains are provided here: **Initial Estimates:** $\hat{\mathbf{R}}_0 = I$, $\hat{\mathbf{b}}_0 = [-3, 2, 4]^T$ and **Estimator Gains:** $W = I_{m\times m}$, $\mathbb{J} = diag([0.09, 0.06, 0.03])$, $\mathbb{M} = diag([0.061, 0.049, 0.0365])$, $\mathbb{D} = diag([2.7, 2.2, 1.5, 0.1, 0.12, 0.14])$, and $\kappa = 0.1$. This was first used on a scenario with no measurement noise. Figures 3.3 and 3.4 present filter results under this scenario.

Observing the results presented in Figures 3.3 and 3.4, the mean estimator collapses down to the truth values within the first 10 seconds of the simulation for the position responses. However, the attitude estimate converges much quicker, on the order of 1 second, Figure 3.5 provides a zoomed in view of this convergence. This converges is maintained throughout the entirety of the simulation, suggesting the velocities are correctly being estimated as well.

Next, a measurement noise value of 1 m was selected to evaluate filter performance under measurement noise. This made the measurement noise matrix $\mathbf{Q} = I$. Figures 3.6 and 3.7 present filter results under this scenario:

From Figures 3.6 and 3.7, the LGVF successfully filters out a majority of the measurement noise for the position estimates with similar converge times to the no noise case. However, there remains a significant level of residual noise in the estimate that remains in a bounded neighborhood about the true value. This suggests the velocity estimates are performing in a similar manner. It must be noted that r_z is blown up. Each dimension shared a similar level of noise post-filtering.

The existence of the noise post-filtering suggests further work be placed on smoothing the estimate after the LGVF, and a requirement for uncertainty quantification. It must also be noted that the existence of noisy estimates does not carry over to the attitude estimate. It is hypothesized that this is a result of solving Wahba's cost function as an optimization problem, and the stochasticity of the estimates are not preserved through the problem. Further work will be required to confirm this hypothesis. While the estimator presents an almost-global asymptotically stable estimator that is robust to measurement noise, it provides no quantification of uncertainty. As a result, in its current form, the estimator cannot be used to make informed decisions. The next chapter discusses implementations and adaptations of this presented estimator to incorporate a quantification on uncertainty.

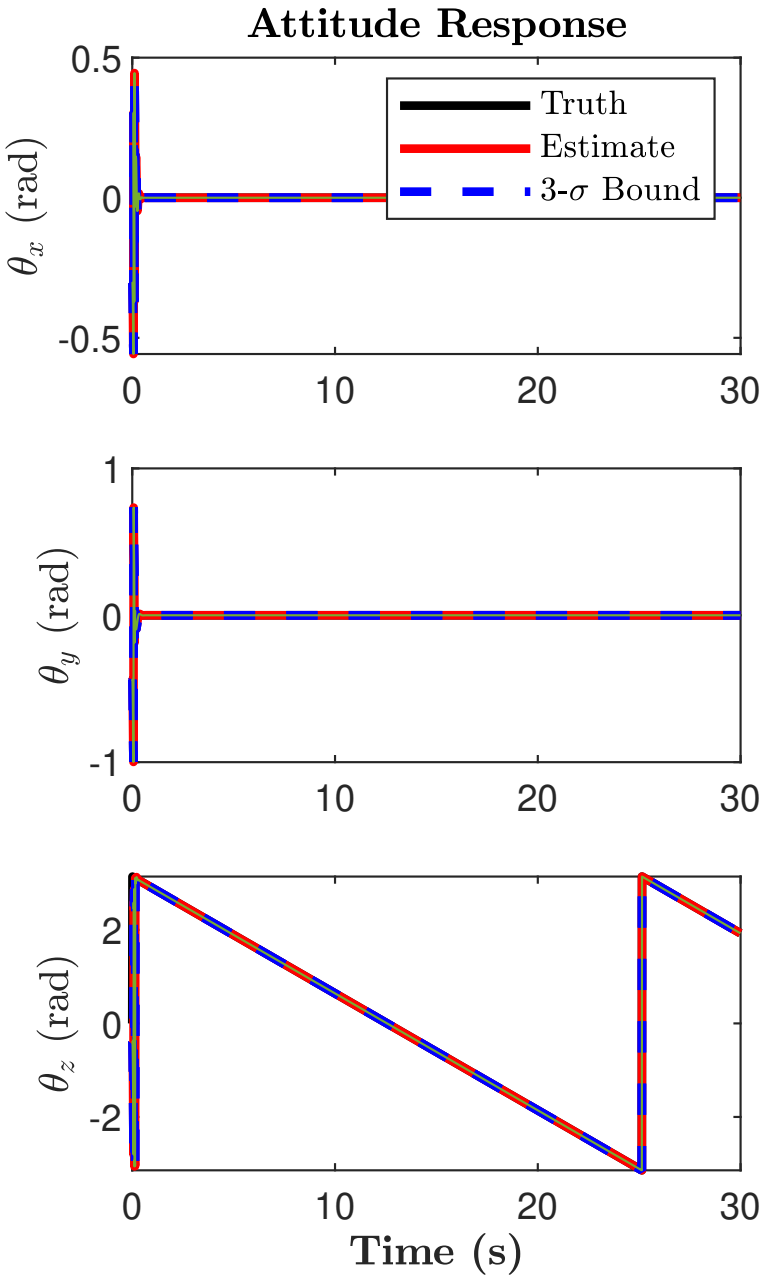

Figure 3.3 No noise mean filter - Attitude Estimate.

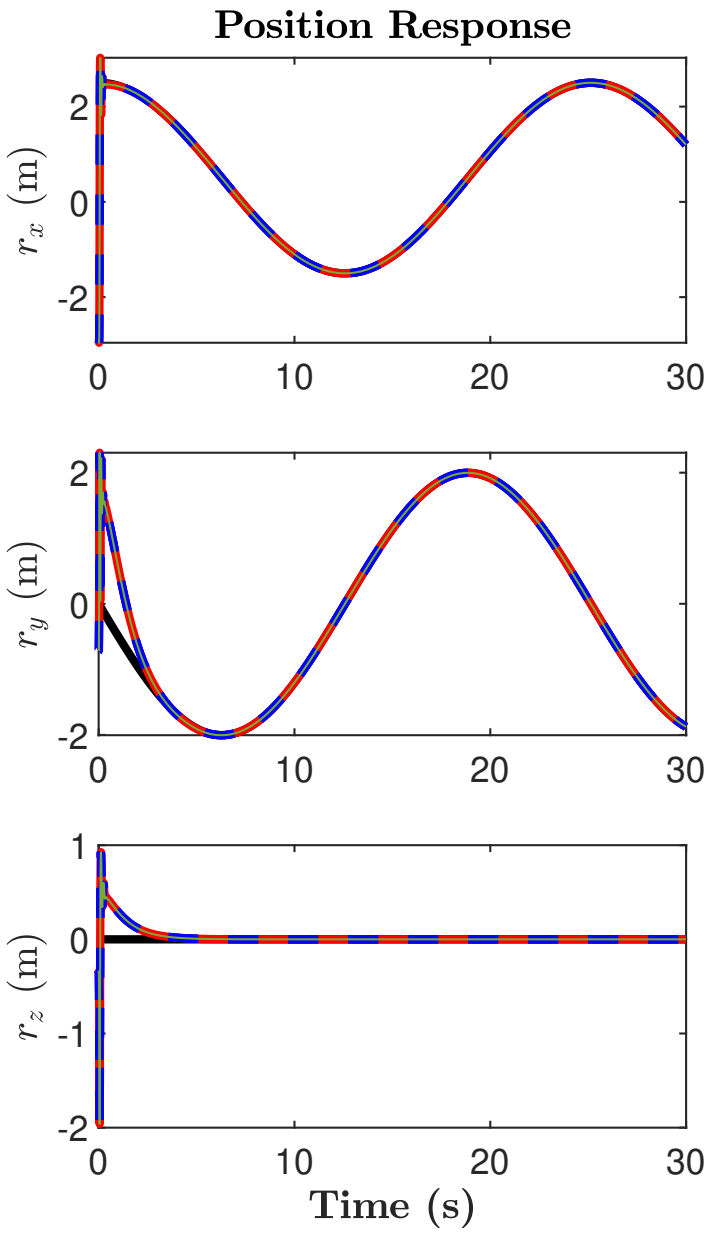

Figure 3.4 No noise mean filter - Position Estimate.

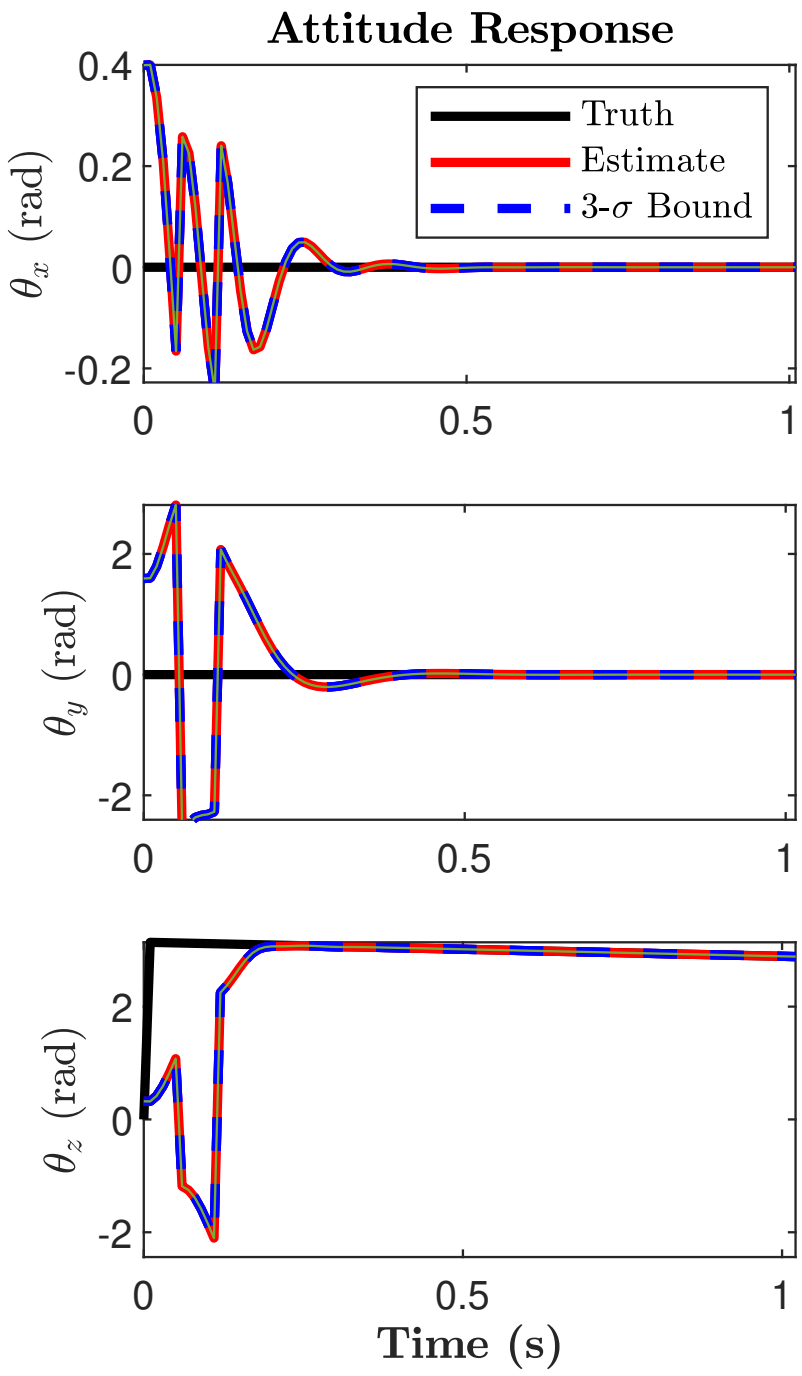

Figure 3.5 Demonstrating the converging properties of the attitude estimate.

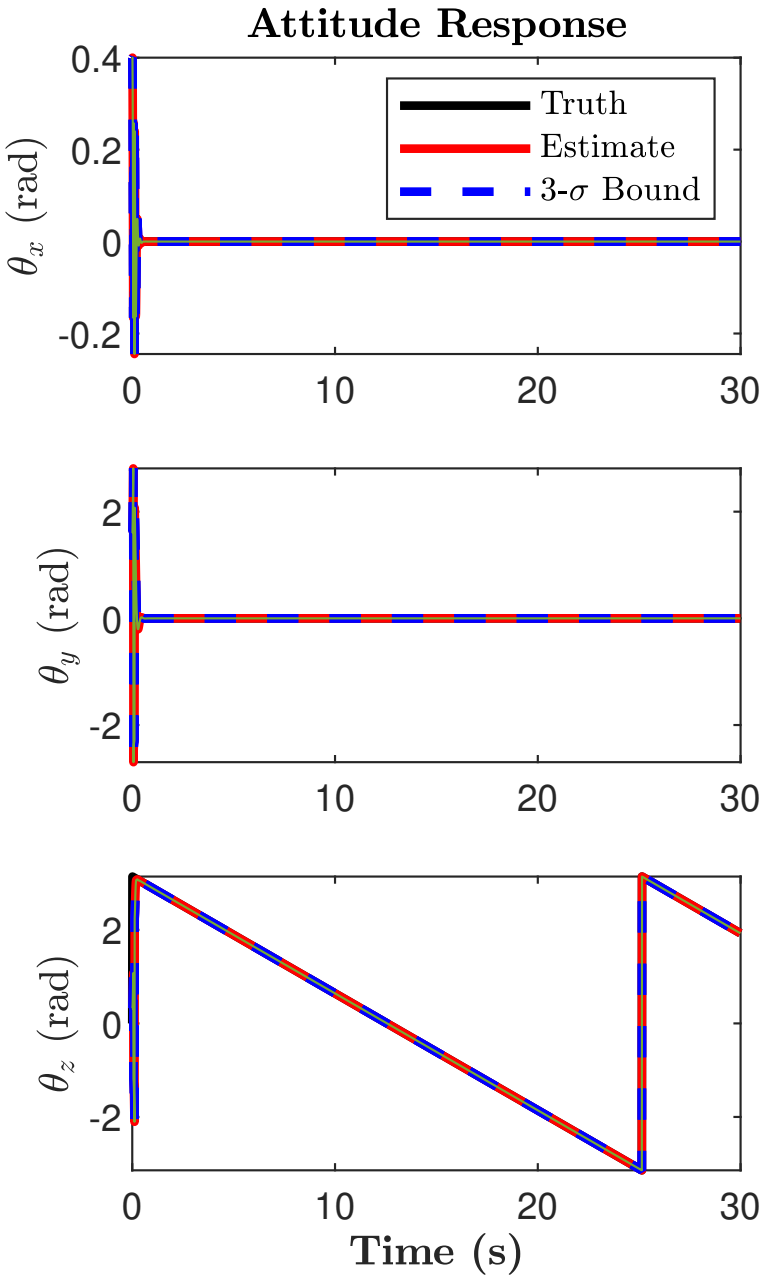

Figure 3.6 Mean Filter Estimate with a noise parameter of 1 meter - Attitude Estimate.

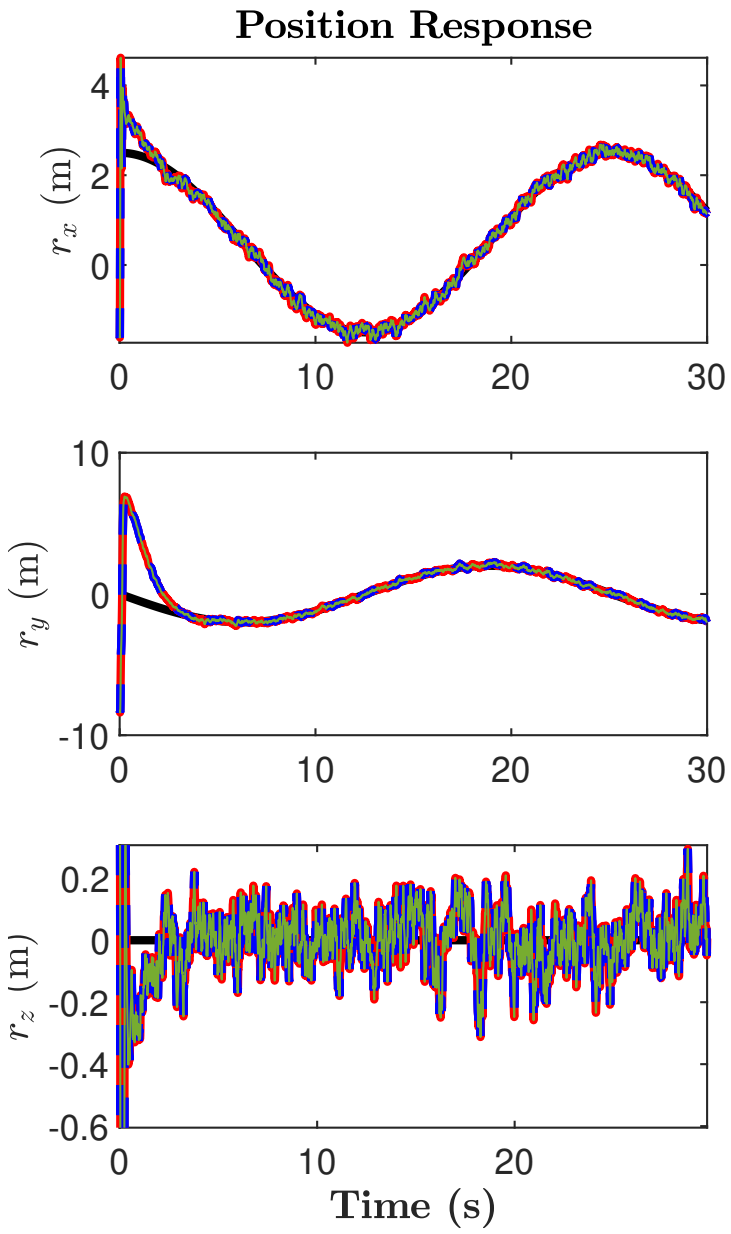

Figure 3.7 Mean Filter Estimate with a noise parameter of 1 meter - Position Estimate.

4. Uncertainty Propagation Implementation

This chapter presents adaptations of the Lie Group Variational Filter to handle uncertainty quantification given a set of vector measurements passed through the LGVF. Methods of uncertainty quantification and propagation are divided into Monte Carlo and Unscented methods. The Monte Carlo methods begin with a significant number of initial estimates each passed through individually through the LGVF to generate both mean and uncertainty estimates. The unscented transformation methods follow the unscented transform algorithm standard in estimation theory to select and propagate initial estimates representative of the true probability distribution.

4.1. Monte Carlo Methods

The Monte Carlo method begins with 100 initial particles. Each particle was randomly selected from within a 6-dimensional hyper-rectangle with outer bounds set by the 3σ uncertainties of the position and attitude expressed as [θ_x, θ_y, θ_z]. This method can be extended to a 12-dimensional hyper-rectangle to incorporate uncertainties in the velocities as well. For computational reasons, and because the interest of this work is the demonstration of the algorithm, only the 6-dimensional version was used. Figure 4.1 gives a visual representation of how the initial estimates are generated. The sampled particles are then placed into $SE(3)$ via the exponential mapping.

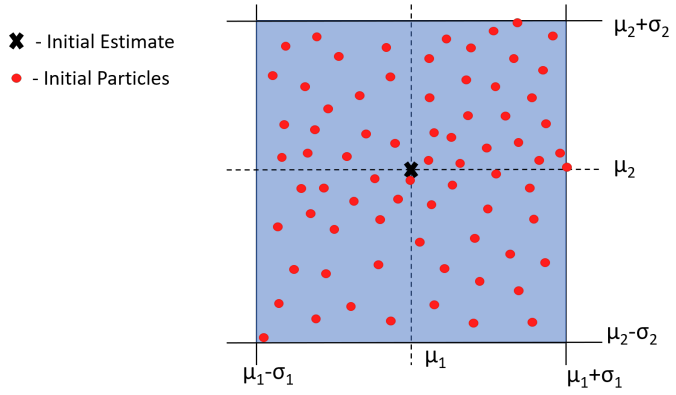

Figure 4.1 Initializing the Monte Carlo distribution using bounding boxes.

Using the same simulated scenario as presented in Section 3.3. combined with the initial particle estimates are then put through the LGVF described in Section 3.2.:

$$\Delta t(J\boldsymbol{\omega}_i)^\times = F_i\mathcal{J} - \mathcal{J}F_i^T \tag{4.1}$$

$$(M + \Delta t\mathbb{D}_t)\boldsymbol{\nu}_{i+1} = F_i^T M\boldsymbol{\nu}_i + \Delta t\kappa(\hat{\mathbf{b}}_{i+1} + \hat{\mathbf{R}}_{i+1}\bar{\mathbf{a}}_{i+1} - \bar{\mathbf{p}}_{i+1}) \tag{4.2}$$

$$\begin{aligned}(J + \Delta t\mathbb{D}_r)\boldsymbol{\omega}_{i+1} =& F_i^T J\boldsymbol{\omega}_i + \Delta t M\boldsymbol{\nu}_{i+1} \times \boldsymbol{\nu}_{i+1} \\ &+ \Delta t\kappa(\hat{\mathbf{b}}_{i+1} + \hat{\mathbf{R}}_{i+1}\bar{\mathbf{a}}_{i+1}) - \Delta t\Phi'(\mathcal{U}_r^0)S_{\Gamma_{i+1}}\end{aligned} \tag{4.3}$$

$$\hat{\mathbf{V}}_i = \hat{\mathbf{V}}_i^m - \mathbf{Ad}_{\hat{\mathbf{T}}_i^{-1}}\boldsymbol{\varphi}_i \tag{4.4}$$

$$\hat{\mathbf{T}}_{i+1} = \hat{\mathbf{T}}_i \exp\left(\Delta t\mathbf{V}_i^\vee\right) \tag{4.5}$$

and applied it to every particle estimate. Each estimate was referenced against the same $\bar{\mathbf{a}}$, $\bar{\mathbf{p}}$ and $\mathbf{V}^m$ to produce the next iteration for that particle. Figures 4.2 and 4.3 shows the results of this Monte Carlo method.

Each particle represents a different estimate throughout the simulation. As the simulation progresses, each particle exhibits a convergence to the true value. Independent of its initialization. This is an attribute of the almost-global asymptotic nature of the filter. As seen with the mean estimators from Figures 3.3, 3.4, 3.6, and 3.7, the position estimate takes a few seconds to converge, while the attitude estimate seems to collapse in under a second. Future work will investigate why this is the case, but, it is again hypothesized this is a result of the optimization problem posed by solving Wahba's cost function. To evaluate the behavior of the estimator towards the end of the simulation, Figures 4.4 and 4.5 presents the final 5 seconds of the simulation.

The almost-global asymptotic stability of the LGVF has presented a problem for uncertainty quantification via a Monte Carlo method. As seen in Figures 4.2 and 4.3, each of the estimates converge to a single estimate. In essence, the estimator becomes 100% confident of the noisy values. This skews the uncertainty quantification as the estimator begins to model the measurement noise on top of the true values. As a result, a direct implementation of the LGVF on an array of initial particle estimates does not correctly portray uncertainty.

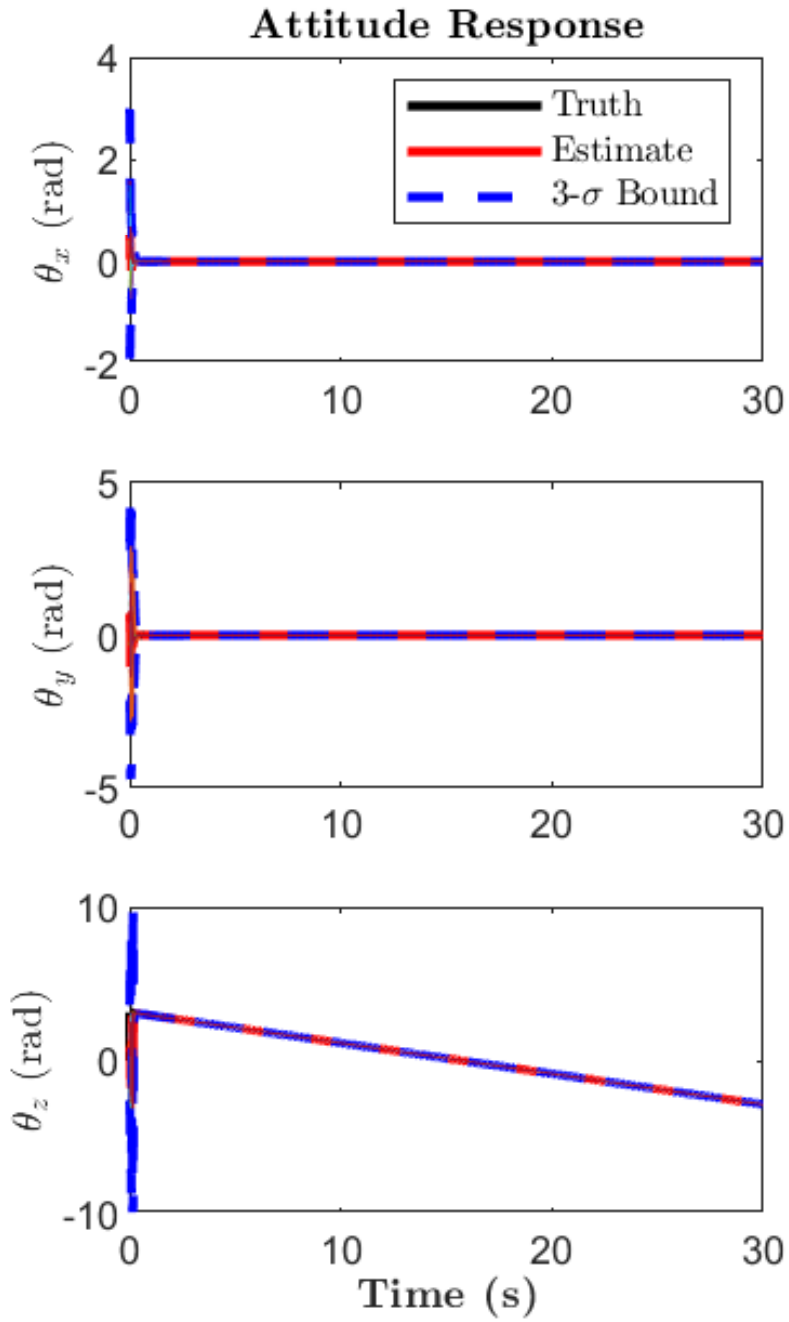

Figure 4.2 Monte Carlo Method attitude estimate results using direct vector measurements.

To accommodate this, the vector measurements were reformulated as Gaussian distributions about the measured vector $\mathbf{a} \sim \mathcal{N}(\mathbf{a}^m, \mathbf{Q})$ where $\mathbf{Q}$ is the measurement covariance matrix. A visualization is provided in Figure 4.6.

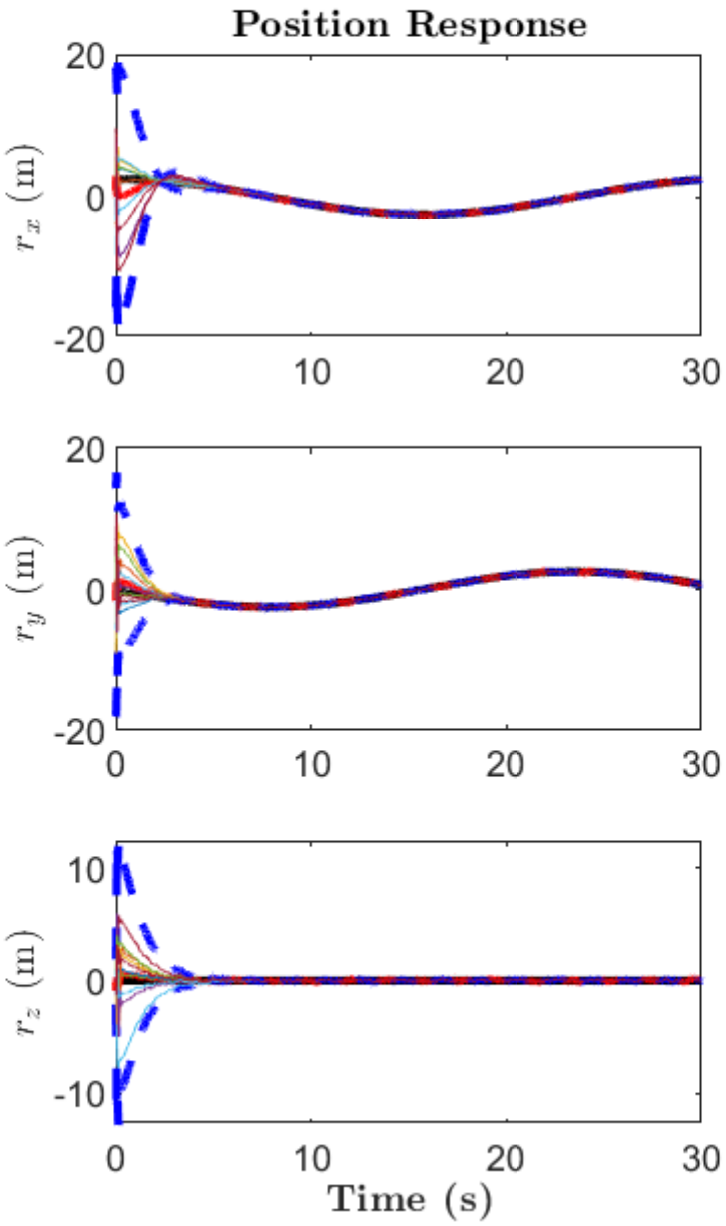

Figure 4.3 Monte Carlo Method position estimate results using direct vector measurements.

So, rather than comparing the estimates to a measured vector, the estimates are referenced to a probability distribution function. As a result, each particle is referenced to a different $\bar{\mathbf{a}}$ within the distribution. This generates different estimates at each time step and the estimates do not converge to the same noisy value, eliminating the problem posed by the

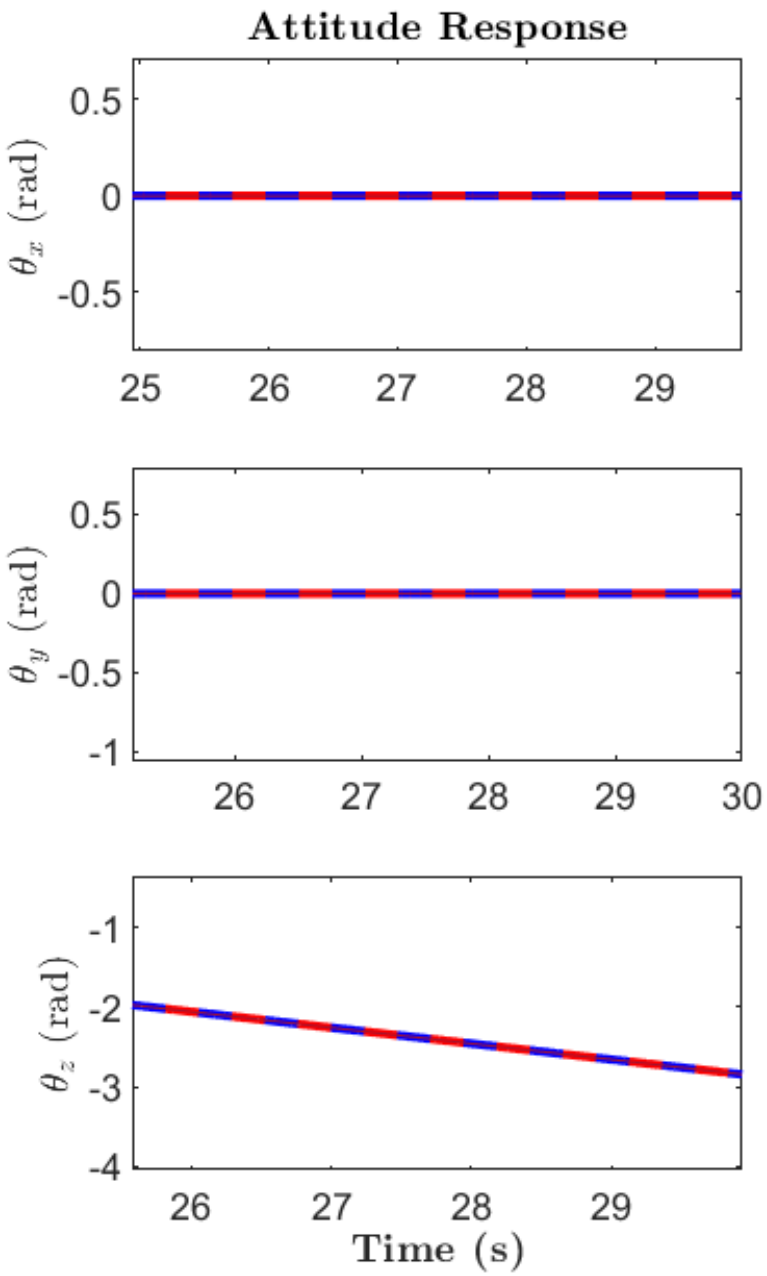

Figure 4.4 Monte Carlo Method attitude estimate results using direct vector measurements. (Zoomed on the last 5 seconds of the simulation)

previous method. The standard deviation of the particle estimates may then be used to quantify the uncertainty. The results of this method are presented in Figures 4.7 and 4.8:

At first glance, the results are very similar to the results observed in Figures 4.2 and 4.3 with marginally more noise in the estimates. However, a zoomed in view of the final 5

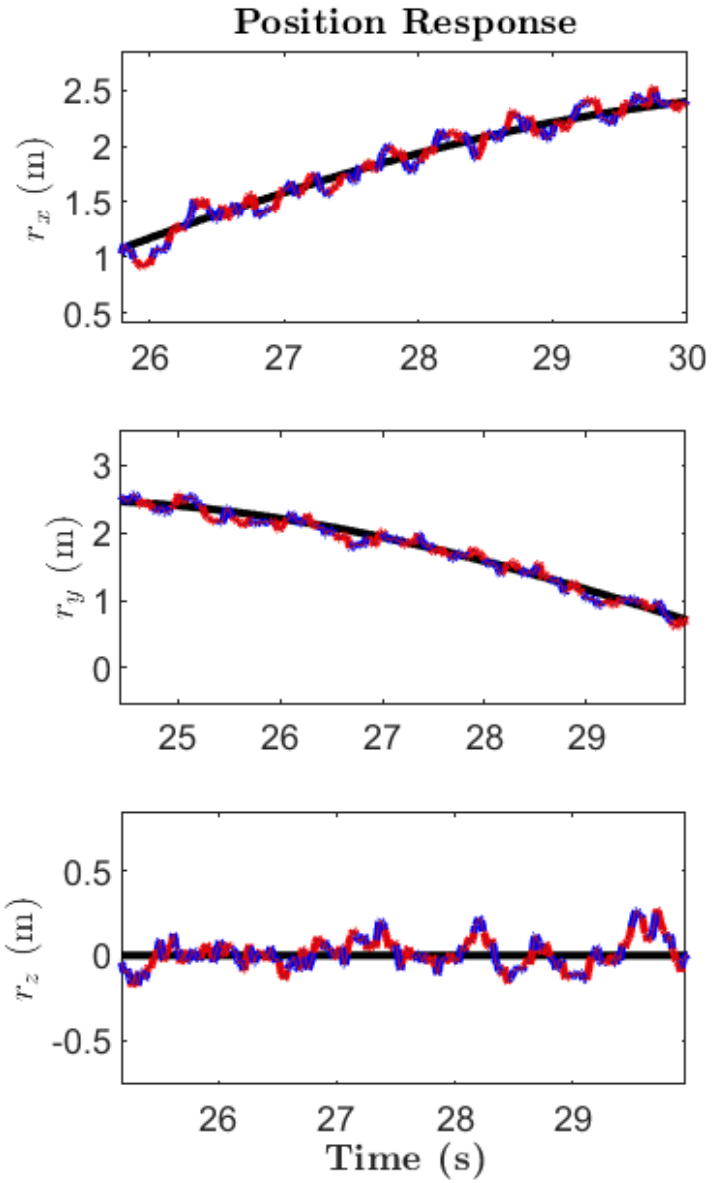

Figure 4.5 Monte Carlo Method position results using direct vector measurements (Zoomed on the last 5 seconds of the simulation).

seconds, seen in Figures 4.9 and 4.10, suggests the small perturbations applied by formulating the measurements as a probability distribution function allows for the uncertainty in the estimates to capture the true value.

According to Figures 4.9 and 4.10, the uncertainty is maintained and does not converge like the previous Monte Carlo method. However, due to the formulation of the LGVF, this

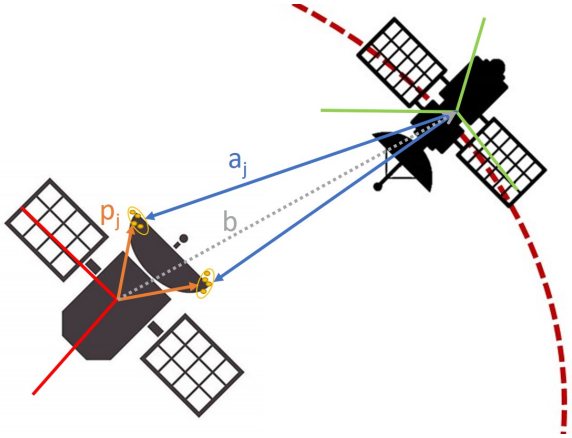

Figure 4.6 Updated measurement with measured features represented as probability distribution functions. This probability distribution function is then sampled for each particle during estimation.

uncertainty is not carried over the attitude parameters. The attitude parameters maintain the convergence of uncertainty over extended periods of time.

Care must be taken using this or similar methods to quantify uncertainty. Because the LGVF uses the mean value of the features in both the map through $\bar{\mathbf{p}}$ and the measurement through $\bar{\mathbf{a}}$, the effect of the probability distribution is diminished as more features are included to obtain the estimate. By nature, the average will go to the truth value as the number of samples tends toward infinity. In this case, this means the amalgamation of the probability distribution functions will tend towards the amalgamation of the measured values and will not produce the desired results. Therefore, the number of particles and the number of features must be taken into account when the evaluating the efficacy of such a method.

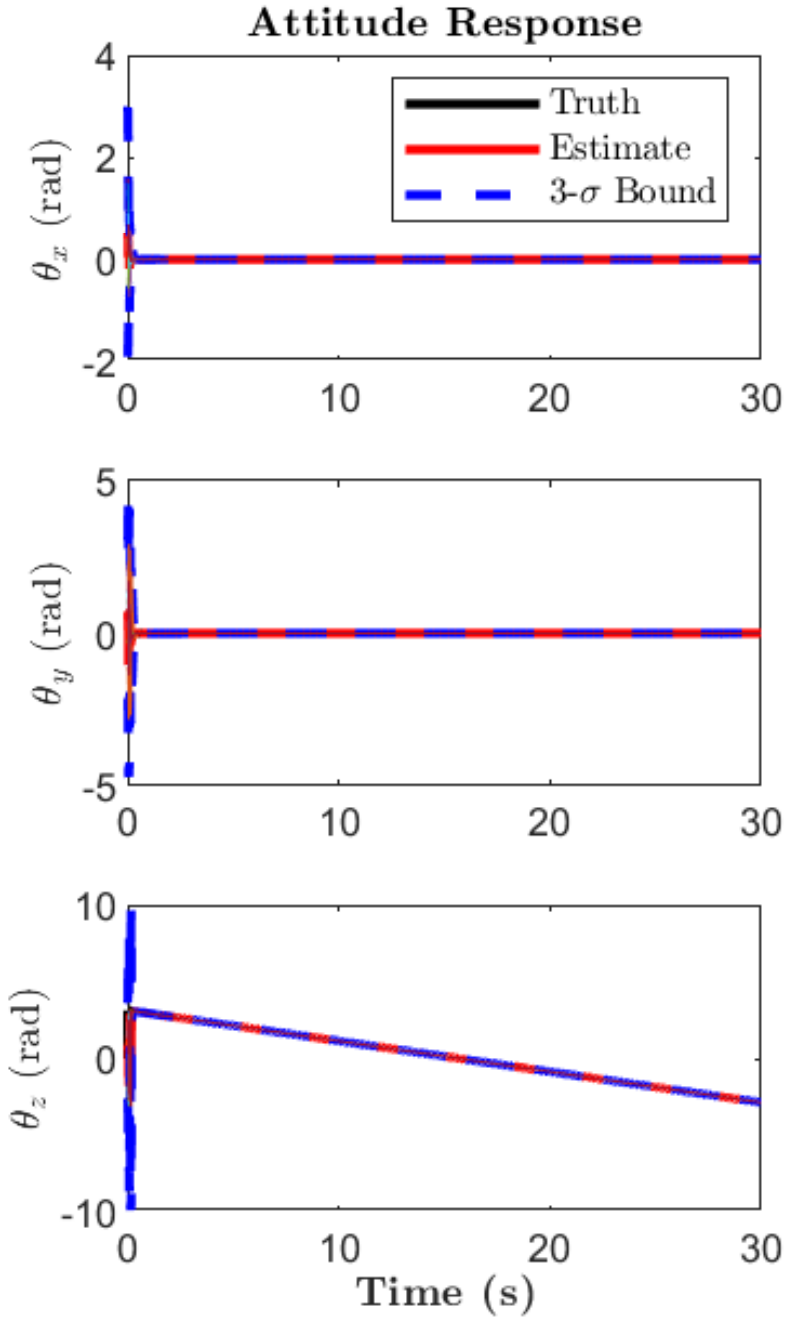

Figure 4.7 Monte Carlo Method attitude estimate results using probability distribution function measurements.

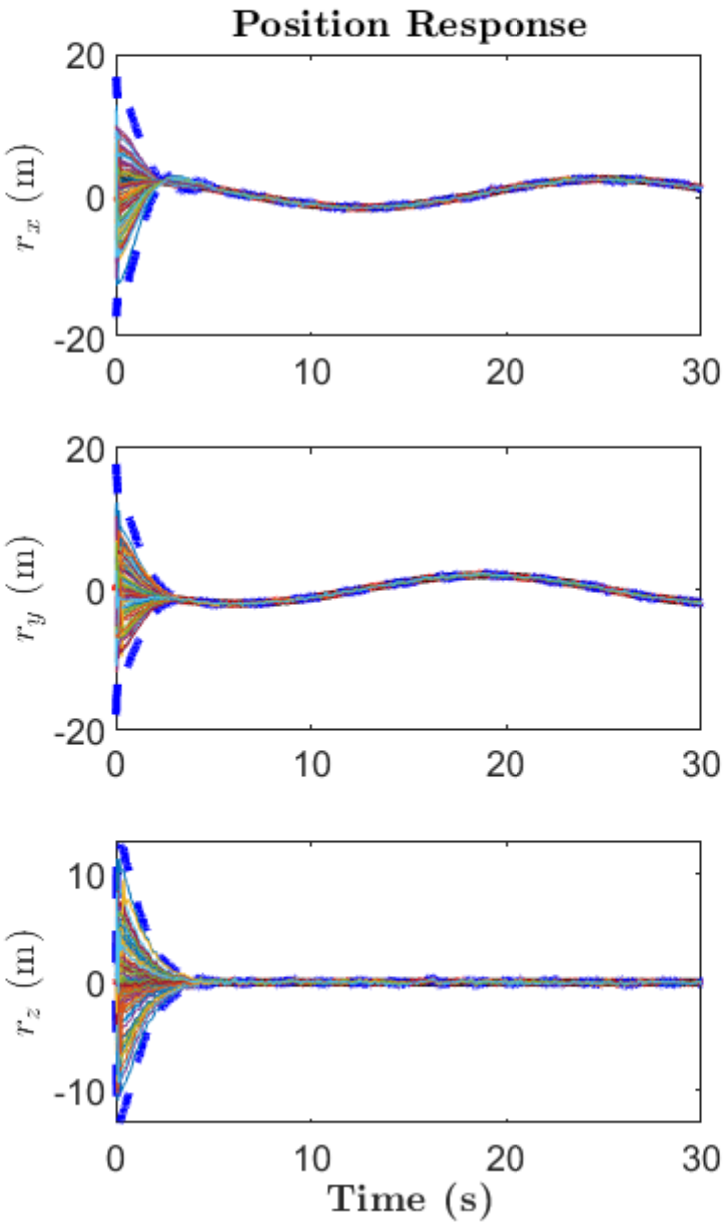

Figure 4.8 Monte Carlo Method position results using probability distribution function measurements

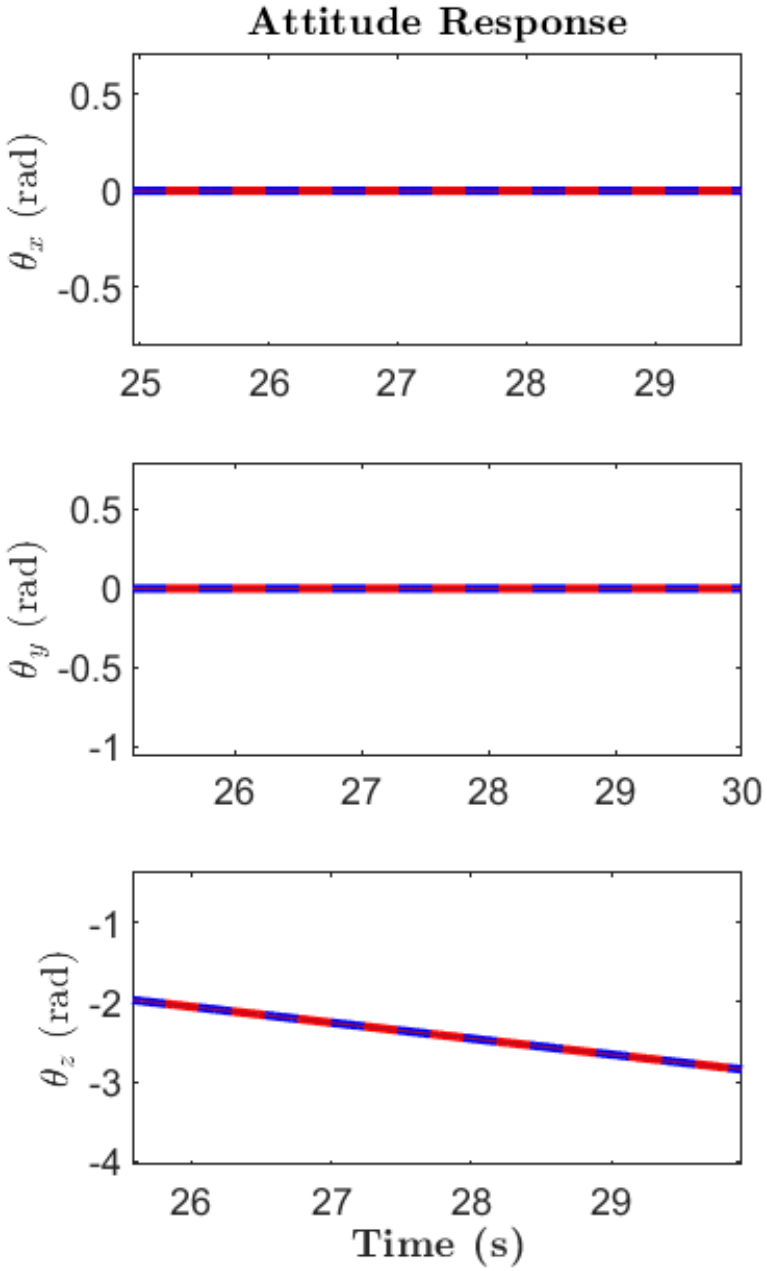

Figure 4.9 Monte Carlo Method attitude estimate results using probability distribution function measurements (Zoomed on the last 5 seconds of the simulation)

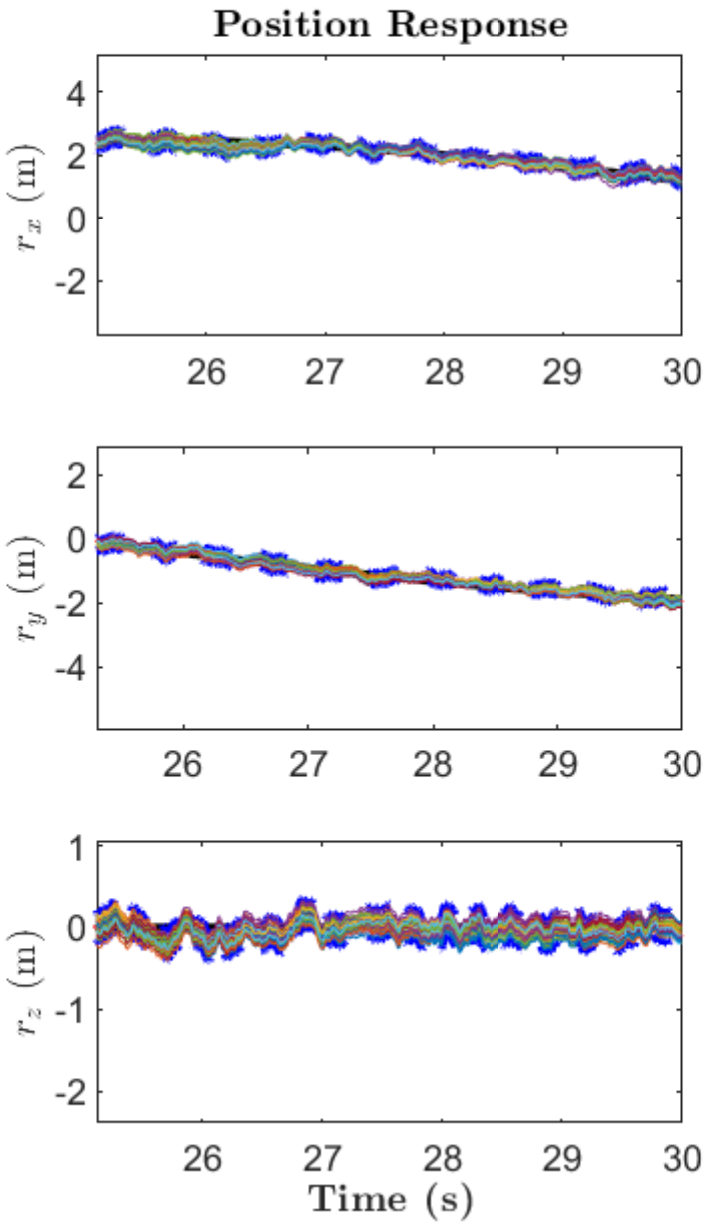

Figure 4.10 Monte Carlo Method position estimate results using probability distribution function measurements (Zoomed on the last 5 seconds of the simulation)

4.2. A Sigma Point Compounding Method

Another approach to quantifying uncertainty is a pose compounding method. Rather than propagating the uncertainty frame an initial frame, assume a small enough timestep that $\mathbf{P}_1 \approx \mathbf{P}_2$ and that $\bar{\mathbf{T}}_{k-1}$ and $\bar{\mathbf{T}}_k$ are given to be the initial mean state estimate and first propagate mean state estimate, respectively. Given each of these elements, the poses and their uncertainties may be compounded to quantify each uncertainty for all additional timesteps. Figure 4.11 gives a visual representation of this process.

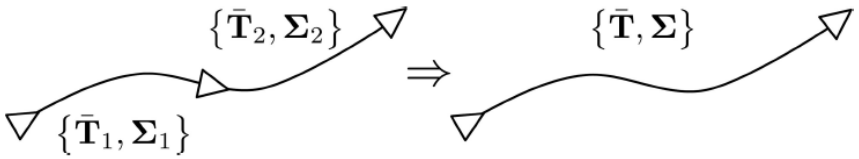

Figure 4.11 Combining Pose and Uncertainty compounds into a singular pose change with associated uncertainty $\mathbf{\Sigma} = \mathbf{P}$ (Barfoot & Furgale, 2014).

Algorithm 1: A SE(3) Pose Uncertainty Compounding Method.

Input : $\bar{\mathbf{T}}_{k-1}$, $\bar{\mathbf{T}}_k$, $\mathbf{P}_{k-1}$, $\mathbf{P}_k$
Output : $\mathbf{P}^+$

1 $\lambda = 1$
2 $\mathbf{S}\mathbf{S}^T = diag\{\mathbf{P}_{k-1}, \mathbf{P}_k\}$
3 $\psi_l = \sqrt{\lambda}\mathbf{S}, l = 1...L$
4 $\psi_{l+L} = -\sqrt{\lambda}\mathbf{S}, l = L+1...2L$
5 $\begin{bmatrix}\xi_{k-1,l} \\ \xi_{k,l}\end{bmatrix} = \psi_l, l = 1...2L$
6 $\mathbf{T}_{k-1,l} = \exp(\xi^{\wedge}_{k-1,l})\bar{\mathbf{T}}_{k-1}$
7 $\mathbf{T}_{k,l} = \exp(\xi^{\wedge}_{k,l})\bar{\mathbf{T}}_k$
8 $\bar{\mathbf{T}} = \bar{\mathbf{T}}_{k-1}\bar{\mathbf{T}}_k$
9 $\xi_l = \log(\mathbf{T}_{k-1,l}\mathbf{T}_{k,l}\bar{\mathbf{T}}^{-1}), l = 1...2L$
10 $\mathbf{P}^+ = \frac{1}{2\lambda}\sum_{l=1}^{2L}\xi_l\xi_l^T$
11

where L is the chosen number of sigma points, in this case is 12. λ is a user defined parameter. Line 2 of the algorithm is solved via Cholesky Decomposition. This method of pose compounding allows for the pose and associated uncertainty to be quantifying over time. However, there is a downfall in the assumption that $\mathbf{P}_{k-1} \approx \mathbf{P}_k$: it is only good for

local approximations and small timesteps. Over time this begins to break down, and is not able to take into account significant decreases in uncertainty due to updated measurements or any other method of improving the state estimate. Figures 4.12 and 4.13 show the results obtained from the Sigma Point method presented in Section 3.B of (Barfoot & Furgale, 2014).

This figure captures an uncertainty, but due to the assumptions can not be definitively declared to be the true uncertainty of the system. Particularly because it does not match the behavior seen in the estimator from Figures 4.7 and 4.8. However, these pose compounding methods may be an interesting method of data and sensor fusion and can be the subject of future work.

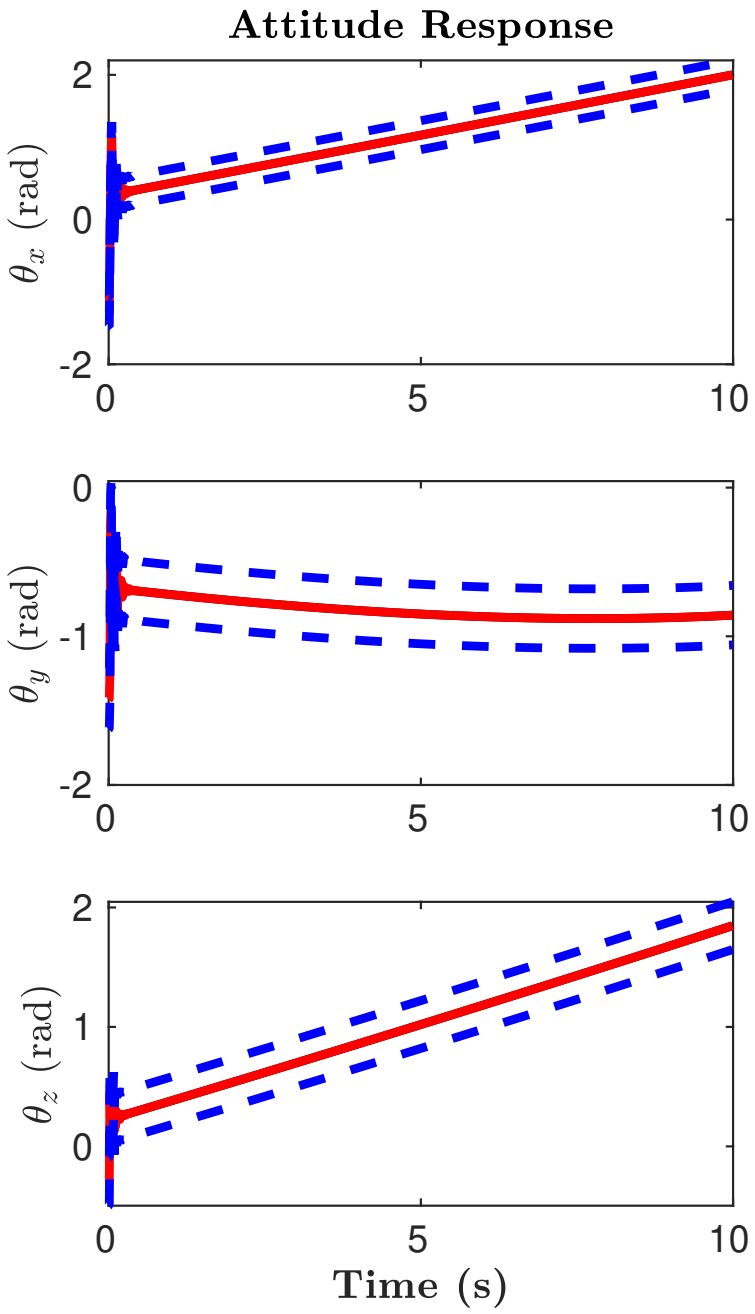

Figure 4.12 Sigma Point Approach attitude estimate results using the method presented by (Barfoot & Furgale, 2014).

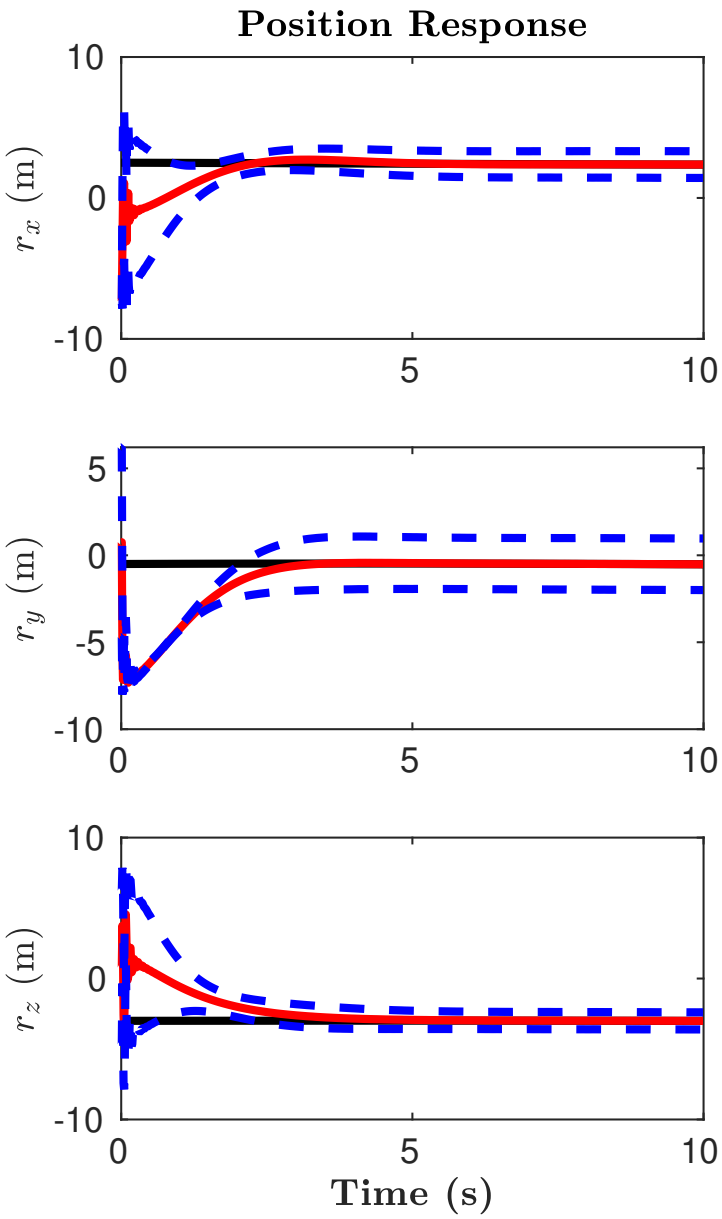

Figure 4.13 Sigma Point Approach position estimate results using the method presented by (Barfoot & Furgale, 2014).

4.3. Unscented Transform

Building on the Sigma Point Compounding Method of the previous sections, an Unscented Transform method can be used. This method is similar to the methods developed in (Brossard et al., 2017) and (Wittal et al., 2021). The measurement function and LGVF estimate for each sigma point are substituted in where typically just a measurement function would be. This allows for each sigma point to be formulated as an element of $SE(3)$.

Algorithm 2: Lie Group Unscented Transform.

Input : $\hat{\boldsymbol{\chi}}_{\boldsymbol{k-1}}, \hat{\boldsymbol{\chi}}_k, \mathbf{P}$
Output : $\mathbf{P}^+$

$\lambda = (\alpha^2 - 1)l$
$\boldsymbol{\alpha_j} = +\text{ chol}((\lambda + l)\mathbf{P}) \quad \forall j = 0, ..., l$
$\boldsymbol{\alpha_j} = -\text{ chol}((\lambda + l)\mathbf{P}) \quad \forall j = l+1, ..., 2l$
$\boldsymbol{\xi} = \boldsymbol{\alpha}$
$\boldsymbol{y}_j = \text{measurement\_function}(\hat{\boldsymbol{\chi}}_k \exp(\boldsymbol{\xi}_j)) \quad \forall j = 0, ..., 2l$
$\hat{\boldsymbol{\chi}}_{\boldsymbol{k}}^{\boldsymbol{j}} = LieGroupVariationalFilter(\hat{\boldsymbol{\chi}}_{\boldsymbol{k-1}}, \boldsymbol{y}_j)$
$\boldsymbol{y}_j = \log(\hat{\boldsymbol{\chi}}_k^j)^\vee$
$\bar{\boldsymbol{y}} = \frac{1}{l}\sum_{j=0}^{2l} \boldsymbol{y}_j$ or $\bar{\boldsymbol{y}} = \log(\hat{\boldsymbol{\chi}}_k)^\vee$
$\mathbf{P}_{yy} = \sum_{j=0}^{2l} (\boldsymbol{y}_j - \bar{\boldsymbol{y}})(\boldsymbol{y}_j - \bar{\boldsymbol{y}})^T$
$\mathbf{P}_{\alpha y} = \sum_{j=0}^{2l} (\boldsymbol{\alpha}_j)(\boldsymbol{y}_j - \bar{\boldsymbol{y}})^T$
$\mathbf{P}^+ = \mathbf{P} - \mathbf{P}_{\alpha y}(\mathbf{P}_{\alpha y}\mathbf{P}_{yy}^{-1})^T$

The algorithm described above presents the currently employed Lie Group Unscented Transform Algorithm, where $\hat{\boldsymbol{\chi}}_{\boldsymbol{k-1}}, \hat{\boldsymbol{\chi}}_{\boldsymbol{k}} \in SE(3)$ are the estimates at their respective time steps. $\mathbf{P}$ is the a priori covariance matrix. The measurement_function() returns a set of vectors corresponding to known features on a map, and the LieGroupVariationalFilter() function returns a pose estimate based on the measurements $\boldsymbol{y}$ and the estimate at previous time step $\hat{\boldsymbol{\chi}}_{\boldsymbol{k-1}}$. From the results presented in Figures 4.14 and 4.15, the covariances exhibit a collapsing behavior towards the true covariances found in Figures 4.7 and 4.8.

However, there are no guarantees the covariance matrix will maintain positive definiteness. It was found that in this simulation the covariance matrix will lose its positive definitiveness about 50 seconds into the simulation. This is a result of the model-free nature of the filter. In typical estimation scenarios the dynamic model will place constraints on the

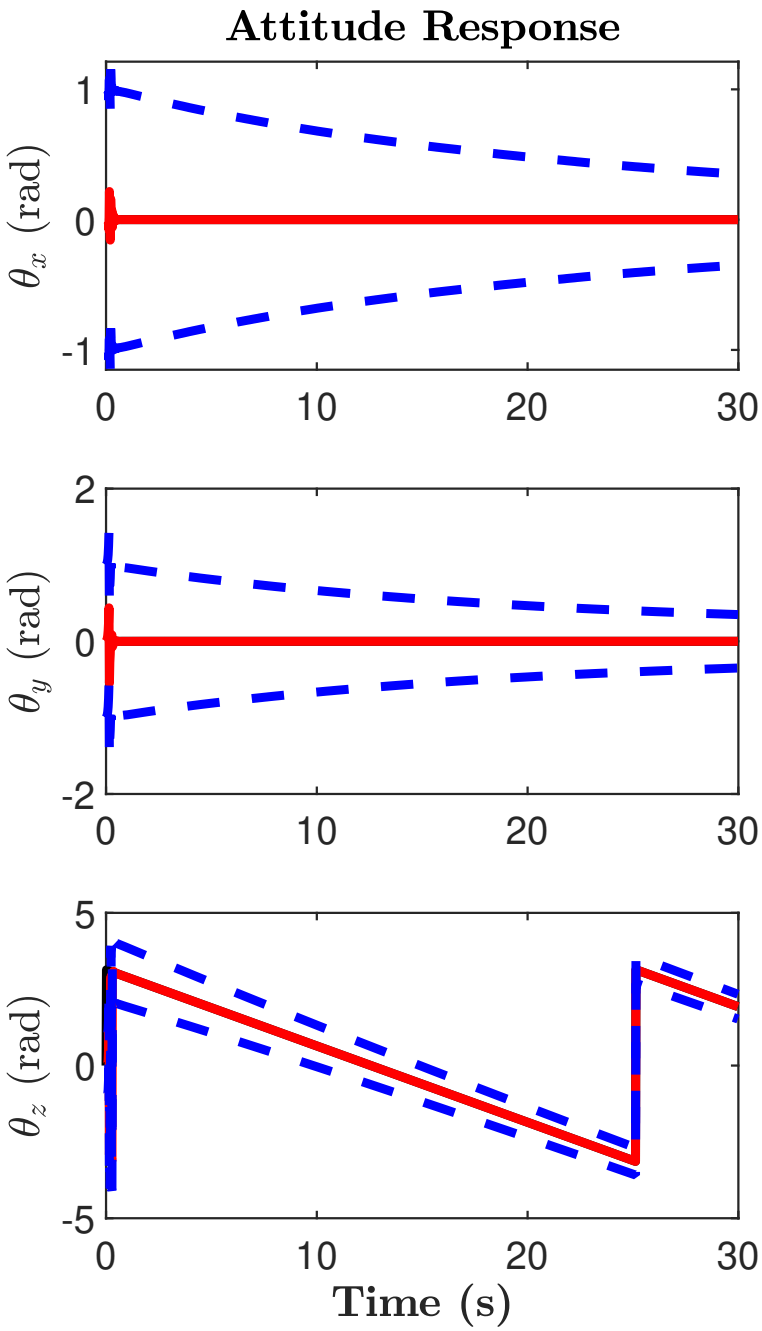

Figure 4.14 Uncertainty in Pose Estimation from the Unscented Transform in Algorithm 1 - Attitude Estimate.

covariance matrix restricting it to be positive definite. The model-free nature of this filter relaxes these constraints and allows for the covariance to lose its positive definitiveness subject to numerical discrepancies. This behavior is a result of numerical imperfection, the

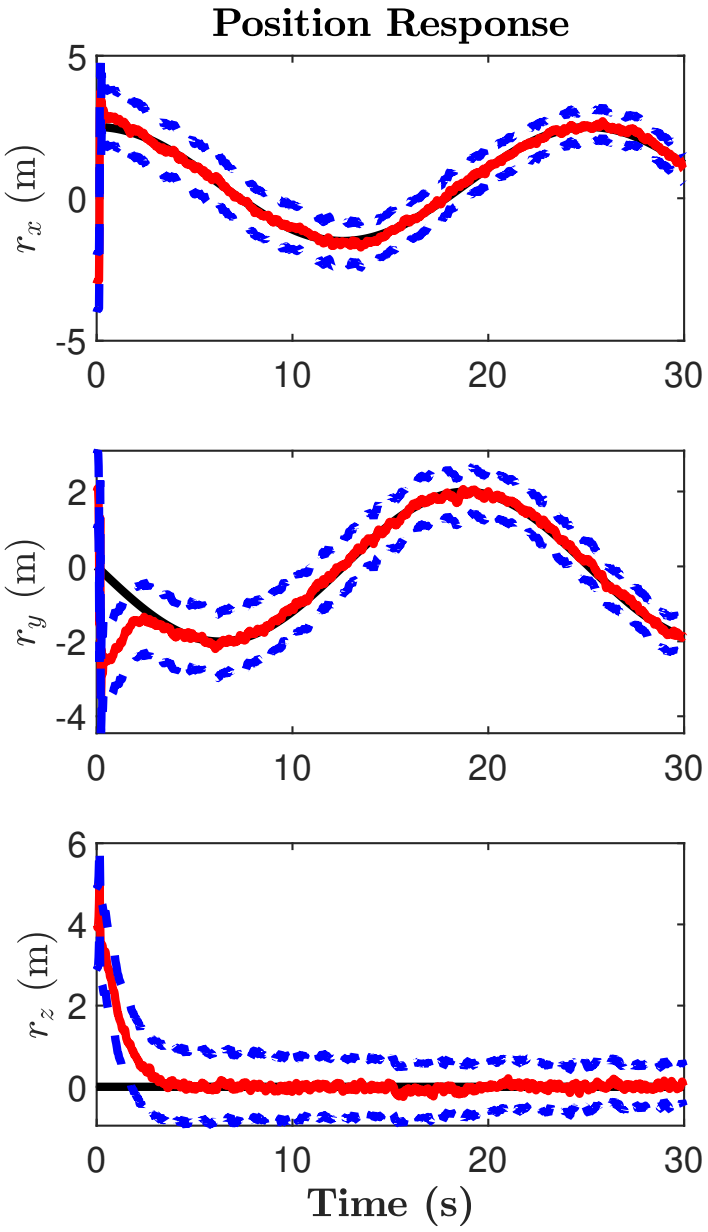

Figure 4.15 Uncertainty in Pose Estimation from the Unscented Transform in Algorithm 1 - Position Estimate

noisy values, that results in the covariance matrix becoming negative as it collapses. This causes a problem in the Cholesky Decomposition and halts any progress being made in the estimation.

Therefore, an alternative method must be put into place to ensure the covariance matrix maintains its positive definitiveness. To fix this issue, Line 12 of Algorithm 3 was included to force the covariance matrix to become positive definite. This line pre-multiplies $\mathbf{P}^{+T}$ to $\mathbf{P}^{+}$ to ensure the resulting quantity is positive. This is analogous to squaring a scalar value. The matrix square root of that value is then taken to retrieve a guaranteed positive form of the matrix. Technically, $x = \pm\sqrt{x^2}$. However, here, only the positive solution is considered for the reasons mentioned previously.

Algorithm 3: Lie Group Unscented Transform.

Input : $\hat{\boldsymbol{\chi}}_{\boldsymbol{k-1}}, \hat{\boldsymbol{\chi}}_k, \mathbf{P}$
Output : $\mathbf{P}^{+}$

1 $\lambda = (\alpha^2 - 1)l$
2 $\boldsymbol{\alpha_j} = +\text{ chol}((\lambda + l)\mathbf{P}) \quad \forall j = 0, ..., l$
3 $\boldsymbol{\alpha_j} = -\text{ chol}((\lambda + l)\mathbf{P}) \quad \forall j = l+1, ..., 2l$
4 $\boldsymbol{\xi} = \boldsymbol{\alpha}$
5 $\boldsymbol{y}_j = \text{measurement\_function}(\hat{\boldsymbol{\chi}}_k \exp(\boldsymbol{\xi}_j)) \quad \forall j = 0, ..., 2l$
6 $\hat{\boldsymbol{\chi}}_{\boldsymbol{k}}^{\boldsymbol{j}} = LieGroupVariationalFilter(\hat{\boldsymbol{\chi}}_{\boldsymbol{k-1}}, \boldsymbol{y}_j)$
7 $\boldsymbol{y}_j = \log(\hat{\boldsymbol{\chi}}_k^j)^{\vee}$
8 $\bar{\boldsymbol{y}} = \frac{1}{l}\sum_{j=0}^{2l} \boldsymbol{y}_j$ or $\bar{\boldsymbol{y}} = \log(\hat{\boldsymbol{\chi}}_k)^{\vee}$
9 $\mathbf{P}_{yy} = \sum_{j=0}^{2l} (\boldsymbol{y}_j - \bar{\boldsymbol{y}})(\boldsymbol{y}_j - \bar{\boldsymbol{y}})^T$
10 $\mathbf{P}_{\alpha y} = \sum_{j=0}^{2l} (\boldsymbol{\alpha}_j)(\boldsymbol{y}_j - \bar{\boldsymbol{y}})^T$
11 $\mathbf{P}^{+} = \mathbf{P} - \mathbf{P}_{\alpha y}(\mathbf{P}_{\alpha y}\mathbf{P}_{yy}^{-1})^T$
12 $\mathbf{P}^{+} = \sqrt{\mathbf{P}^{+T}\mathbf{P}^{+}}$

The results of this method are presented in Figures 4.16 and 4.17. The behavior of the attitude and position estimates from Figures 4.14 and 4.15 is replicated with this method. Uncertainty in the attitude estimate is quantified, in contrast to the behavior of the Monte Carlo methods. The attitude estimates remain smooth as seen in the previous sections, while the position estimates maintain residual noise levels post-filtering. This behavior is consistent to what is observed in previous sections.

This simulation was run for 80 seconds to ensure that by forcing the covariance matrix to remain positive allowed for the filtering to continue past the point where the previous method failed. In Figures 4.18 and 4.19, it is observed that the covariances converge similarly to the covariances found in the Monte-Carlo method.

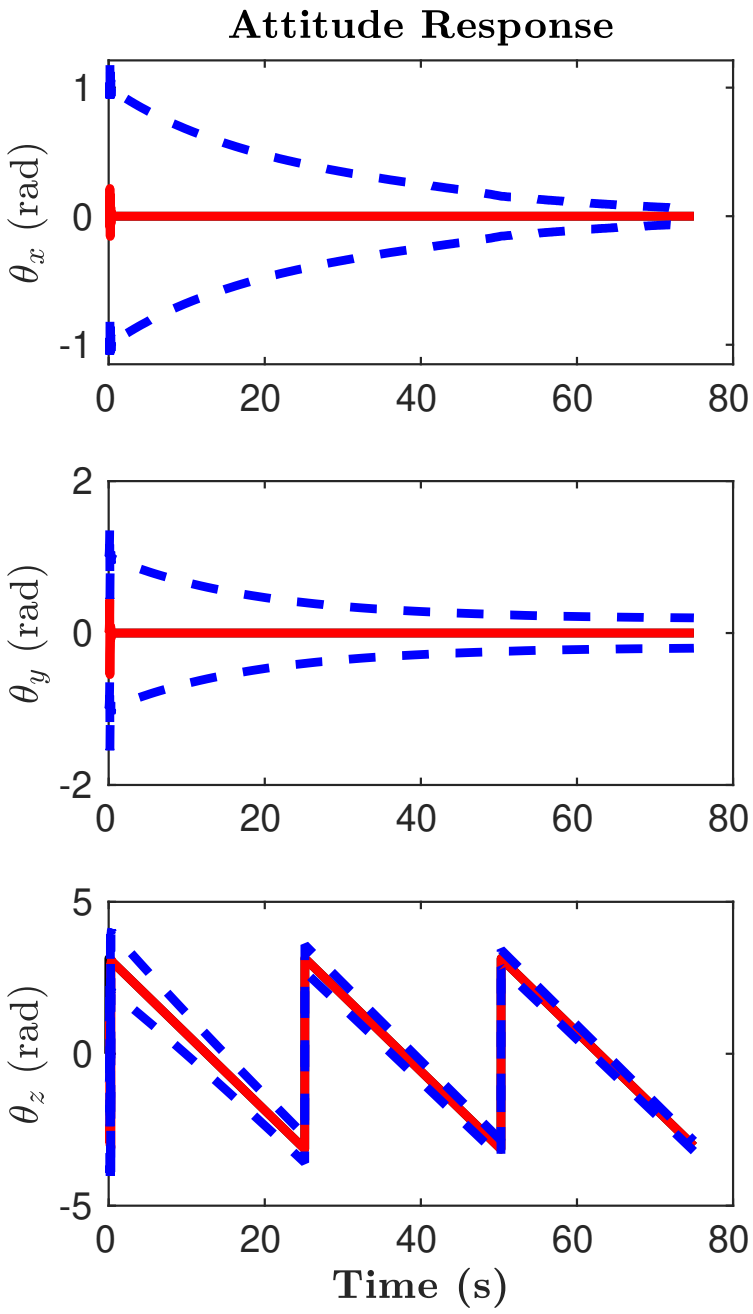

Figure 4.16 UKF Force Positive Definite - Attitude Estimate.

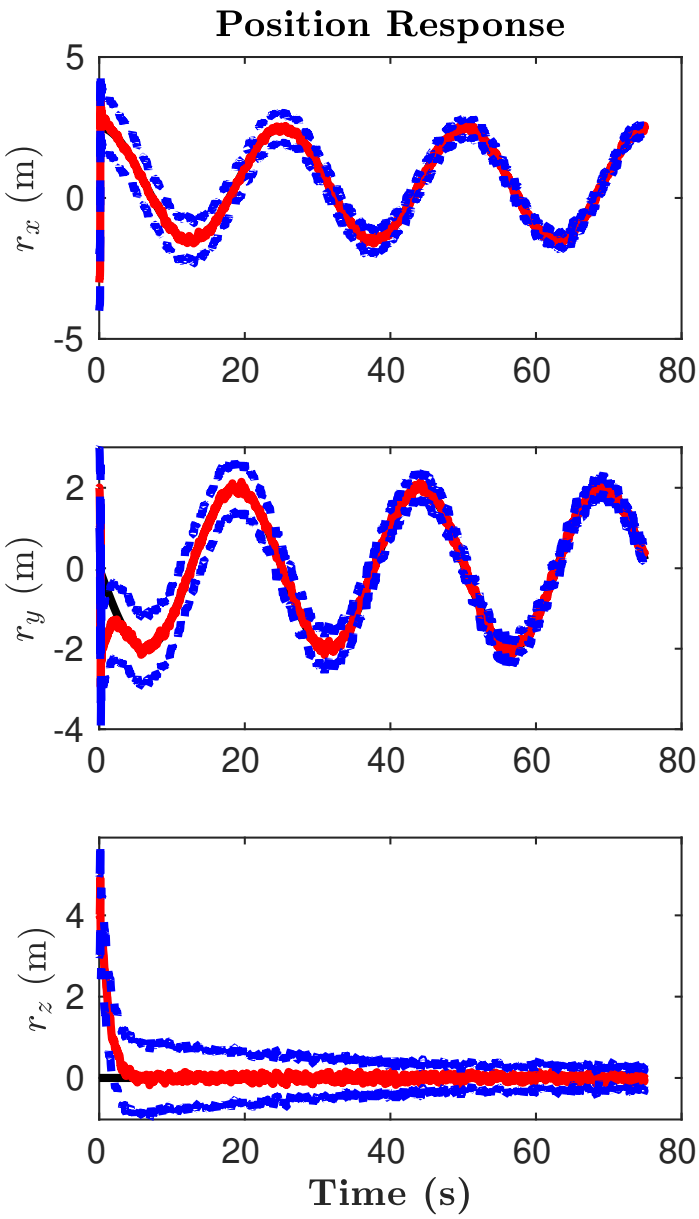

Figure 4.17 UKF Force Positive Definite - Position Estimate.

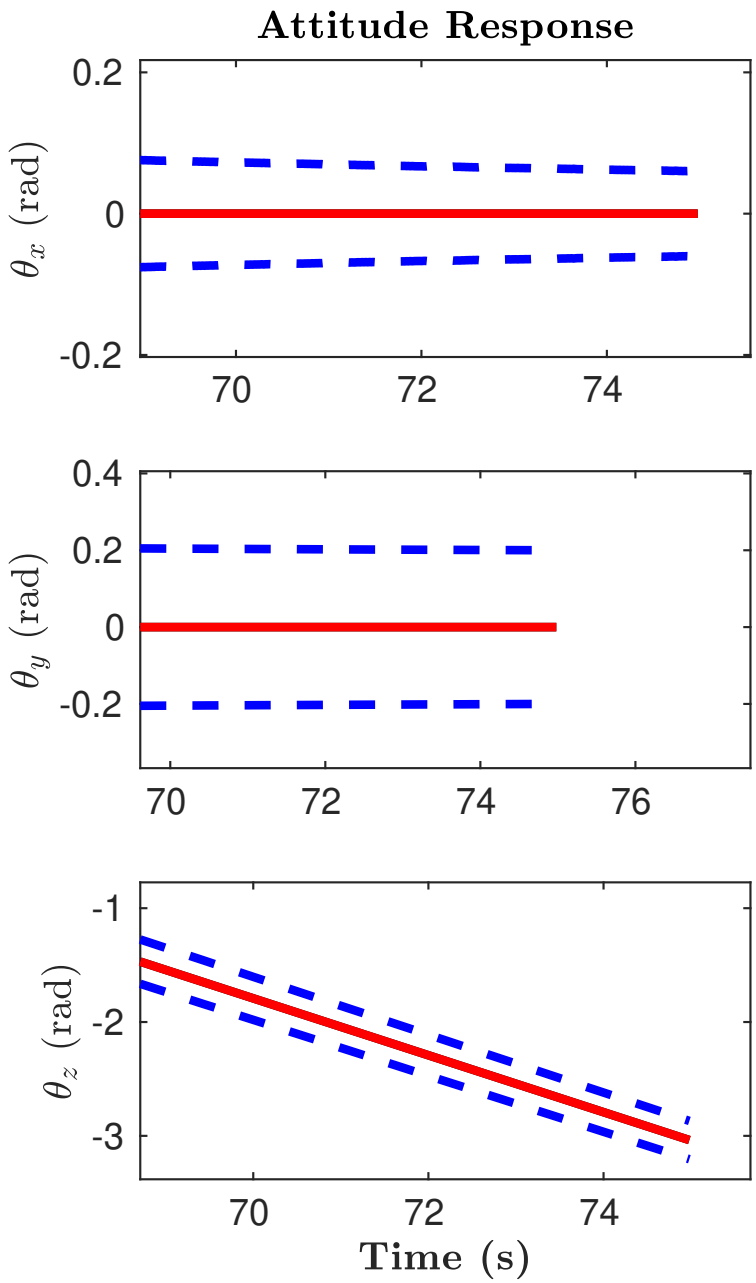

Figure 4.18 UKF Force Positive Definite - Attitude Estimate (Zoomed in to last 5 seconds).

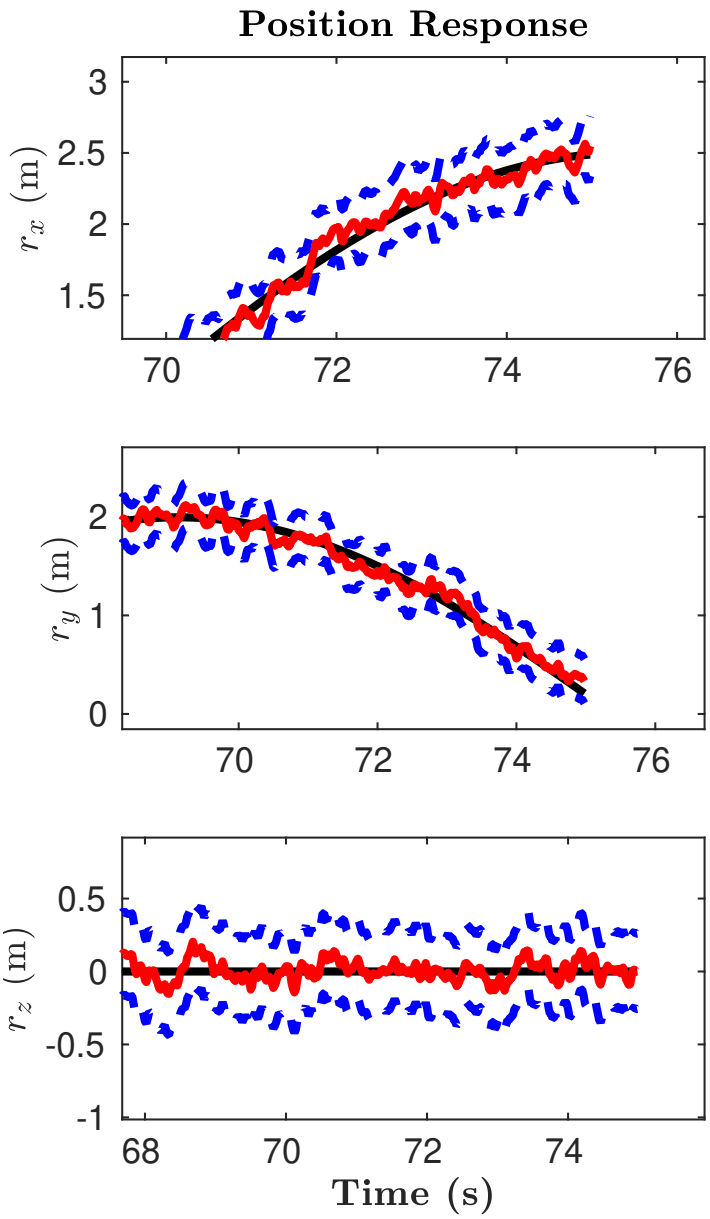

Figure 4.19 UKF Force Positive Definite - Position Estimate (Zoomed in to last 5 seconds).

5. Conclusions and Future Work

In conclusion, the enclosed work presents a methodology to capture uncertainty built around the Lie Group Variational Filter developed in (Izadi & Sanyal, 2016). The implementation of Monte Carlo and Unscented methods are presented and discussed.

The Monte Carlo methods provide a baseline to which the Unscented methods may be compared for capturing uncertainty. Because the LGVF can be thought of more as a dynamics model than a true estimation scheme, this process is analogous to the standard methods of evaluating uncertainty characterization against a Monte Carlo approach.

The Monte Carlo approaches while providing a good baseline, are not computationally efficient for implementation and, furthermore, do not seem to capture uncertainty in the attitude estimates over extended amounts of time. This is a result of the measurement model being developed from strictly vector measurements of feature positions and there associated velocities.

On the other hand, the unscented methods are more computationally efficient due to the strategic selection of particles, or sigma points, to be used in the estimator. This significant decrease in particle number allows for the estimator to quantify uncertainty in a way that collapse to the steady-state uncertainty presented in the Monte Carlo method.

However, as mentioned in Chapter 1, this thesis provides a foundation on which the author intends to build from. This leaves significant opportunities for future work and development for estimation on the $SE(3)$ for real applications. The authors recommendation for topics of future work include but are not limited to:

- Updated measurement models to more closely match measurements seen through cameras or other visual sensor.
- The use of optical flow or another computer vision scheme to measure relative velocities.
- Development of a method of data fusion to include multiple measurement sources and their associated uncertainties.

- Development of a hybrid model-free and model-based estimator to take leverage the advantages presented by both schemes.
- Evaluate the performance of the estimator under control actuations.
- Development of smoother to eliminate any residual noise present in the mean state estimate

REFERENCES

Barfoot, T. D., & Furgale, P. T. (2014). Associating uncertainty with three-dimensional poses for use in estimation problems. *IEEE Transactions on Robotics*, *30*(3), 679–693.

Barnouin, O., Daly, M., Palmer, E., Johnson, C., Gaskell, R., Al Asad, M., ... others (2020). Digital terrain mapping by the osiris-rex mission. *Planetary and Space Science*, *180*, 104764.

Bay, H., Tuytelaars, T., & Van Gool, L. (2006). Surf: Speeded up robust features. In *European conference on computer vision* (pp. 404–417).

Brossard, M., Bonnabel, S., & Condomines, J.-P. (2017). Unscented kalman filtering on lie groups. In *2017 ieee/rsj international conference on intelligent robots and systems (iros)* (pp. 2485–2491).

Cardoso, J. R., & Leite, F. S. (2003). The moser–veselov equation. *Linear algebra and its applications*, *360*, 237–248.

Dennehy, C., & Carpenter, I. (2006). Demonstration of autonomous rendezvous technology mishap investigation board review. *NASA ESC, Tech. Rep. RP-06-119*.

Dennehy, C. J., & Carpenter, J. R. (2011). A summary of the rendezvous, proximity operations, docking, and undocking (rpodu) lessons learned from the defense advanced research project agency (darpa) orbital express (oe) demonstration system mission.

Holland, D. (2002). 6.4. 1 a case study of the near-catastrophic mir-progress 234 collision with emphasis on the human factors/systems-level issues surrounding this mishap. In *Incose international symposium* (Vol. 12, pp. 820–827).

Ivanov, T., Huertas, A., & Carson, J. M. (2013). Probabilistic hazard detection for autonomous safe landing. In *Aiaa guidance, navigation, and control (gnc) conference* (p. 5019).

Izadi, M., Samiei, E., Sanyal, A. K., & Kumar, V. (2015). Comparison of an attitude estimator based on the lagrange-d'alembert principle with some state-of-the-art filters. In *2015 ieee international conference on robotics and automation (icra)* (pp. 2848–2853).

Izadi, M., & Sanyal, A. K. (2016). Rigid body pose estimation based on the lagrange–d'alembert principle. *Automatica*, *71*, 78–88.

Kelso, T., et al. (2009). Analysis of the iridium 33 cosmos 2251 collision.

Lee, T., Leok, M., & McClamroch, N. H. (2007). Lie group variational integrators for the full body problem in orbital mechanics. *Celestial Mechanics and Dynamical Astronomy*, *98*(2), 121–144.

Lee, T., & Leve, F. (2014). Lagrangian mechanics and lie group variational integrators for spacecraft with imbalanced reaction wheels. In *2014 american control conference* (pp. 3122–3127).

Leok, M. (2007). An overview of lie group variational integrators and their applications to optimal control. In *International conference on scientific computation and differential equations* (p. 1).

Lindeberg, T. (2012). Scale invariant feature transform.

Lovelly, T. M., Wise, T. W., Holtzman, S. H., & George, A. D. (2018). Benchmarking analysis of space-grade central processing units and field-programmable gate arrays. *Journal of Aerospace Information Systems*, *15*(8), 518–529.

Mangelson, J. G., Ghaffari, M., Vasudevan, R., & Eustice, R. M. (2020). Characterizing the uncertainty of jointly distributed poses in the lie algebra. *IEEE Transactions on Robotics*, *36*(5), 1371–1388.

Mark, C. P., & Kamath, S. (2019). Review of active space debris removal methods. *Space Policy*, *47*, 194–206.

Mur-Artal, R., Montiel, J. M. M., & Tardos, J. D. (2015). Orb-slam: a versatile and accurate monocular slam system. *IEEE transactions on robotics*, *31*(5), 1147–1163.

Nakath, D., Clemens, J., & Rachuy, C. (2019). Active asteroid-slam. *Journal of Intelligent & Robotic Systems*, 1–31.

Nordkvist, N., & Sanyal, A. K. (2010). A lie group variational integrator for rigid body motion in se (3) with applications to underwater vehicle dynamics. In *49th ieee conference on decision and control (cdc)* (pp. 5414–5419).

Reesman, R., & Rogers, A. (2018). Getting in your space: Learning from past rendezvous and proximity operations. *Aerospace Corporation, May*.

Sanyal, A. K., Izadi, M., & Butcher, E. (2014). Determination of relative motion of a space object from simultaneous measurements of range and range rate. In *2014 american control conference* (pp. 1607–1612).

Sanyal, A. K., Izadi, M., Scheeres, D. J., Misra, G., & Samiei, E. (2014). Estimation of dynamics of space objects from visual feedback during proximity operations. In *Aiaa/aas astrodynamics specialist conference* (p. 4419).

Schlenker, L., Moretto, M., Gaylor, D., & Linares, R. (2019). Simultaneous localization and mapping for satellite rendezvous and proximity operations using random finite sets.

Setterfield, T. P. (2017). *On-orbit inspection of a rotating object using a moving observer* (Unpublished doctoral dissertation). Massachusetts Institute of Technology.

Sola, J., Deray, J., & Atchuthan, D. (2018). A micro lie theory for state estimation in robotics. *arXiv preprint arXiv:1812.01537*.

Wittal, M. M., Mangiacapra, G., Appakonam, A., Nazari, M., & Capello, E. (2021). Stochastic spacecraft navigation and control in lie group se(3) around small irregular bodies..

Yamaguchi, T., Saiki, T., Tanaka, S., Takei, Y., Okada, T., Takahashi, T., & Tsuda, Y. (2018). Hayabusa2-ryugu proximity operation planning and landing site selection. *Acta Astronautica*, *151*, 217–227.

Yoshimitsu, T., Kawaguchi, J., Hashimoto, T., Kubota, T., Uo, M., Morita, H., & Shirakawa, K. (2009). Hayabusa-final autonomous descent and landing based on target marker tracking. *Acta Astronautica*, *65*(5-6), 657–665.